The Martian daytime convective boundary layer: Results from radio occultation measurements and a mesoscale model

The Martian daytime convective boundary layer: Results from radio occultation measurements and a mesoscale model

D. P. Hinson[a,b,*], D. Tyler Jr.[c], S. R. Lewis[d], M. Pätzold[e], S. Tellmann[e], B. Häusler[f], G. L. Tyler[b]

[a] *Carl Sagan Center, SETI Institute, Mountain View, CA 94043, USA*
[b] *Department of Electrical Engineering, Stanford University, Stanford, CA 94305, USA*
[c] *College of Earth, Ocean, and Atmospheric Sciences, Oregon State University, Corvallis, OR 97331, USA*
[d] *Department of Physical Sciences, The Open University, Walton Hall, Milton Keynes MK7 6AA, UK*
[e] *Rheinisches Institut für Umweltforschung, Universität Zu Köln, Cologne, Germany*
[f] *Institut für Raumfahrttechnik und Weltraumnutzung, Universität der Bundeswehr München, Neubiberg, Germany*

Abstract

We investigate the behavior of the Martian daytime convective boundary layer (CBL) through a combination of data analysis and modeling. This study relies on two subsets of Mars Express radio occultation (RO) measurements that sounded the atmosphere in northern spring of successive Mars years. Only the first year of observations has been examined previously (Hinson et al., 2008); the second year provides complementary spatial coverage and greatly increases the total number of observations. Analysis of the RO profiles yields basic characteristics of the CBL, such as its depth D and the average potential temperature of the mixed layer θ_m. We also combine RO retrievals of surface pressure with surface temperatures from infrared sounding to characterize the surface forcing, expressing the result as a potential temperature θ_s. These observations are at local times in early afternoon for θ_s and late afternoon for θ_m and D, when each parameter is near its diurnal maximum. We use measurements at mid-to-low latitudes, which sample a wide range of θ_s (227–294 K), to determine the response of the lower atmosphere to spatial variations in surface forcing. The depth of the CBL ranges from less than 3 km in the midlatitude topographic basins to more than 9 km above elevated terrain in the tropics. The dependence of θ_m on θ_s is linear, with a characteristic slope of about 0.7 in both years. We gain further insight by performing a simulation with the Oregon State University Mars Mesoscale Model in a re-

gion centered on Isidis Planitia, which includes two potential landing sites for the Mars 2020 Rover. As expected from previous modeling of much smaller craters, the arc of steep topography along the western and southern margins of Isidis produces a distinctive, diurnally varying, mesoscale circulation. The simulation captures key features of the observations, such as the wide variations in θ_m and D — by 34 K and 9 km, respectively — that occur within this region. The model also accounts for peculiar features of RO profiles on the rim of Isidis, where the wind field strongly influences the depth and diurnal evolution of the CBL. Detailed comparisons with the observations validate the general performance of the model and confirm several aspects of the simulated wind field.

Keywords: Mars, atmosphere; Atmospheres, dynamics; Occultations; Radio observations

---

*Corresponding Author: David P. Hinson, Carl Sagan Center, SETI Institute, 189 Bernardo Ave., Mountain View, CA 94043, USA; Email, dhinson@seti.org; Phone, 650-810-0217

1. Introduction

The lower atmosphere of Mars is strongly affected by its interaction with the surface within a region known as the planetary boundary layer (PBL). The daytime depth of the PBL is largely determined by the response of the atmosphere to solar heating of the surface, which produces a convective boundary layer (CBL) whose properties vary strongly with time of day, location, and season. Vertical transport of heat and momentum by the CBL has a large impact on the temperature structure and circulation of the atmosphere; the CBL also modulates the spatial distributions of dust and water. See Petrosyan et al. (2011) or Read et al. (2017) for a review of PBL physics, observations, and modeling.

This paper uses a combination of data analysis and modeling to investigate the daytime structure and dynamics of the lower atmosphere. The data set includes 114 atmospheric profiles retrieved from Mars Express (MEx) radio occultation (RO) measurements (Pätzold et al., 2016). A complementary numerical simulation is performed by the Oregon State University (OSU) Mars Mesoscale Model (MMM) (Tyler et al., 2002). This approach yields new insight into the behavior of the CBL, including its response to spatial variations in surface forcing and its modification by the topographic circulation in the Isidis region. The results reported here are a substantial extension of previous work in this area. We not only examine a much larger number of RO measurements than Hinson et al. (2008) but also present the results in a more informative way. In addition, mesoscale modeling allows us to interpret the observations in the context of a realistic simulation of the topographic circulation, which adds considerably to what has been learned from large-eddy simulations (Spiga et al., 2010a,b).

The MEx RO measurements are essential to this investigation for two reasons. First, atmospheric profiles retrieved from these data have a vertical resolution of about 500 m, sufficient for determining the structure and stability of the lower atmosphere (Hinson et al., 2008) and an order of magnitude beyond the capabilities of infrared sounders (Conrath et al., 2000; Kleinböhl et al., 2009). Moreover, the MEx orbit drifts in local time, providing systematic RO coverage of the tropics in late afternoon, when the CBL has reached its

maximum depth. Only a handful of RO measurements were obtained under these conditions by the Viking Orbiters (Lindal et al., 1979). For both Mars Global Surveyor (MGS) and Mars Reconnaissance Orbiter (MRO), RO coverage at low latitudes is restricted by their sun synchronous orbits to predawn local times of 3–5 h (Hinson and Wilson, 2004; Hinson et al., 2014).

The OSU MMM has been used to investigate diverse aspects of mesoscale meteorology on Mars, such as the transient eddies that appear at high northern latitudes during northern summer (Tyler and Barnes, 2005) and the complex, diurnally varying circulation at Gale Crater (Tyler and Barnes, 2013). The MMM has also played an important role in planning NASA missions to the surface of Mars, including both Phoenix (Tyler et al., 2008) and Mars Science Laboratory (Vasavada et al., 2012); similar work is underway in connection with landing site selection for the Mars 2020 Rover (https://mars.nasa.gov/mars2020/). In these mission-oriented applications, the MMM performs high resolution numerical simulations to predict the atmospheric conditions that will be encountered as the vehicle descends to the surface and to evaluate the likelihood of landing safely and accurately. One important objective of this paper is to validate the MMM in a context relevant to Mars 2020.

The first half of the paper discusses the RO observations. Section 2 reviews the coverage of the RO data used here and the general characteristics of the retrieved atmospheric profiles. Section 3.1 explains the procedure for analyzing the RO profiles; the measured properties of the CBL are listed in Section 3.2. Section 4 presents a variety of results, including typical characteristics of the CBL (Section 4.1), the effect of fronts on the temperature structure at midlatitudes (Section 4.2), the response of the atmosphere to variations in surface forcing (Section 4.3), and anomalous structure observed at several locations (Section 4.4).

The second half of the paper focuses on the OSU MMM. Section 5 describes the configuration of the model. We perform a simulation at moderate spatial resolution in northern midspring in a region centered on Isidis Planitia, a large impact basin with a diameter of more than 1000 km. This is an appealing target for several reasons: the atmospheric circulation and dynamics are inherently interesting, reasonably good RO coverage is available, and the region includes two potential landing sites for Mars 2020, which will arrive at Mars in

early spring. After validating the simulation through detailed comparisons with RO profiles (Section 6.1), we use the model to explore aspects of the diurnally varying circulation that cannot be observed directly (Section 6.2). A close comparison between the simulation and two peculiar RO profiles illustrates the impact of the wind field on the depth and diurnal evolution of the CBL. More generally, the Isidis regional study is a continuation of previous efforts to model the mesoscale circulation associated with Isidis (Rafkin and Michaels, 2003) and more compact craters such as Gusev (Toigo and Richardson, 2003; Rafkin and Michaels, 2003) and Gale (Tyler and Barnes, 2013). The paper closes with a summary of the main results in Section 7.

We adopt standard conventions for time keeping on Mars. The term "sol" denotes the mean solar day of 88,775 s. Local time is expressed in solar hours (24 per sol). The time of year is denoted by L_s, the angular position of Mars in its orbit about the Sun, with $L_s = 0°$ at the vernal equinox of the northern hemisphere. We follow Clancy et al. (2000) in assigning numbers to Mars years (MY), such that MY01 began on 11 April 1955.

2. Experiment description

Mars Express has been performing RO observations of the Martian ionosphere and neutral atmosphere since 2004. The methodology and the results obtained in the first 10 years of the mission are reviewed by Pätzold et al. (2016). This section describes the coverage and basic characteristics of the RO profiles used in this investigation.

2.1. Spatial and temporal coverage

We consider two sets of RO measurements that sampled the atmospheric structure under similar conditions in successive Mars years. The first set comprises 32 profiles from midspring of MY27 ($L_s = 44$–$70°$) at latitudes from 28°N to 14°S and local times of 17.0–17.2 h. The second set comprises 82 profiles extending from late winter of MY27 to midspring of MY28 ($L_s = 357$–$43°$) at latitudes from 55°N to 4°S; the local time drifted from 14.0 h at the start of the interval to 15.9 h at the end. For simplicity we use MY28 to denote the second set of observations. Fig. 1 shows the spatial coverage of these measurements superimposed on

a map of surface topography from the MGS Mars Orbiter Laser Altimeter (MOLA) (Smith et al., 2001).

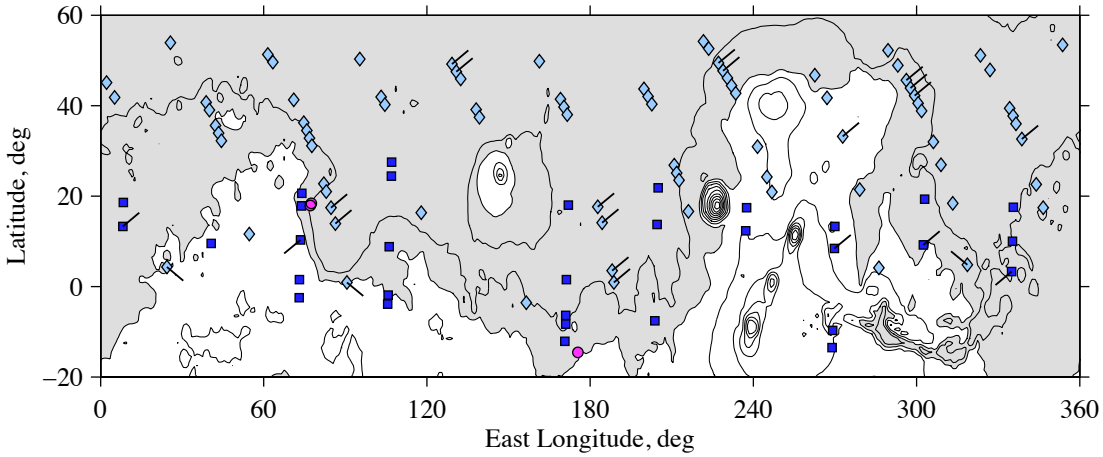

Figure 1: Locations of the MEx RO measurements used in this paper. The observations are from northern spring of MY27 (dark blue squares) and MY28 (light blue diamonds). Pink circles denote the locations of the three potential landing sites for Mars 2020. Contours of surface elevation are shown at intervals of 2.5 km, with grey shading for negative values. Diagonal lines mark the locations of the profiles that appear in Figs. 2, 4–7, 9, and 10. The direction of the lines has no significance; some lines have been rotated for clarity.

In both MY27 and MY28 the RO measurements progressed from north to south, drifting southward at a rate of 0.8° of latitude per sol in MY27 and 0.6° per sol in MY28. At the time of these observations MEx completed 11 orbits in 3.0 sols, which limits the zonal coverage to 11 equally spaced longitudes. Hence, pairs of observations separated by 11 orbits sample the atmosphere at nearly the same location, with an offset in latitude of about 2°.

Table 1 lists the names and locations of the three landing sites currently under consideration for Mars 2020, which will arrive at Mars near $L_s = 6°$ (in February 2021) and land at a local time of about 15 h (https://mars.nasa.gov/mars2020/). These locations are indicated in Fig. 1. The RO coverage is better near Jezero (JEZ) and NE Syrtis (NES) than at Columbia Hills (CLH). (While this paper was under review, NASA selected Jezero as the landing site, though further study is required before the decision is final.)

Table 1
Locations of potential landing sites for Mars 2020.

Name	Site Code	East Longitude (°)	Latitude (°)
Jezero	JEZ	77.5	+18.4
NE Syrtis	NES	77.2	+17.9
Columbia Hills	CLH	175.4	−14.6

2.2. Attributes of RO profiles

We retrieved atmospheric profiles from raw data products that are available at the Planetary Science Archive (PSA) of the European Space Agency. Each observation yields a profile of temperature T and pressure p versus planetocentric radius r that extends from about 1 km above the surface to about 45 km altitude, a pressure range of about 5–700 Pa (Hinson et al., 2008). The vertical resolution is about 500 m. The profiles are most accurate near the surface, where the standard deviations of temperature σ_T and pressure σ_p are typically 0.3 K and 1 Pa, respectively. The fractional uncertainties σ_T/T and σ_p/p increase steadily with altitude by a factor of about 2.2 per pressure scale height (about 10 km). We plan to deliver these profiles to the PSA beginning in 2019.

The retrieval algorithm solves for the radius r, east longitude λ, and latitude ϕ associated with each sample of T and p (Hinson et al., 1999). The uncertainty in position is about 25 m in both the vertical and horizontal directions, commensurate with the accuracy of the orbit reconstructions (Rosenblatt et al., 2008), so that the profiles can be registered accurately within the gravity field of Mars. Throughout this paper we adopt a vertical coordinate in which altitude z is measured relative to the equipotential surface that serves as the reference for Martian topography (Smith et al., 2001). In midspring, the pressure at $z = 0$ is about 600 Pa.

The limb sounding geometry limits the horizontal resolution along the spacecraft-to-Earth direction. A radio signal traverses an atmospheric layer of depth d in a distance $L \approx 2(2\,r_m\,d)^{1/2}$, where r_m is the radius of Mars. When d is 5 km, the typical depth of the CBL, L is 370 km, equivalent to a 6° arc of a great circle. The horizontal resolution in the

direction perpendicular to the line of sight is comparable to the vertical resolution.

3. Characterization of the CBL

Basic properties of the CBL can be derived through analysis of the RO profiles. This section describes the methodology and applies it to the observations from MY27 and MY28.

3.1. Method of analysis

It is convenient to express the RO profiles in terms of potential temperature θ, defined as (Gill, 1982):

$$\theta = T\,(p_o/p)^{R/c_p}\ . \tag{1}$$

The ratio of the gas constant R to the specific heat at constant pressure c_p is about 0.25 under the conditions considered here. We set the reference pressure p_o to 610 Pa. By definition, θ is constant within a layer of neutral static stability, where the lapse rate of T is adiabatic.

Fig. 2 illustrates the method of analysis using a pair of profiles from MY28. One is from Tempe Terra and the other is from Acidalia Planitia, where the surface elevation is 4.7 km lower. Both profiles contain a distinct CBL at low altitudes, where θ is nearly constant. In the free air above the mixed layer θ increases steadily with increasing altitude, indicating stable stratification.

With few exceptions, the RO profiles exhibit an abrupt transition from nearly neutral stability in the CBL to stable stratification in the overlying free air, as illustrated by the pair of profiles in Fig. 2C. In both cases, $d\theta/dz$ increases from less than 1 K km^{-1} to more than 2 K km^{-1} within a vertical distance of less than 500 m. We define the top of the CBL as the midpoint of this transition, where $d\theta/dz = 1.5$ K km^{-1}. The definition is somewhat arbitrary but yields reasonable results, as shown in subsequent figures.

We determined z_t, the altitude at the top of the CBL, from linear interpolation between adjacent samples of $d\theta/dz$. We then computed D, the depth of the CBL, by subtracting the elevation at the surface from z_t. We also computed θ_m, the average value of θ within the mixed layer, with each sample given equal weight. Both D and θ_m are smaller for the profile

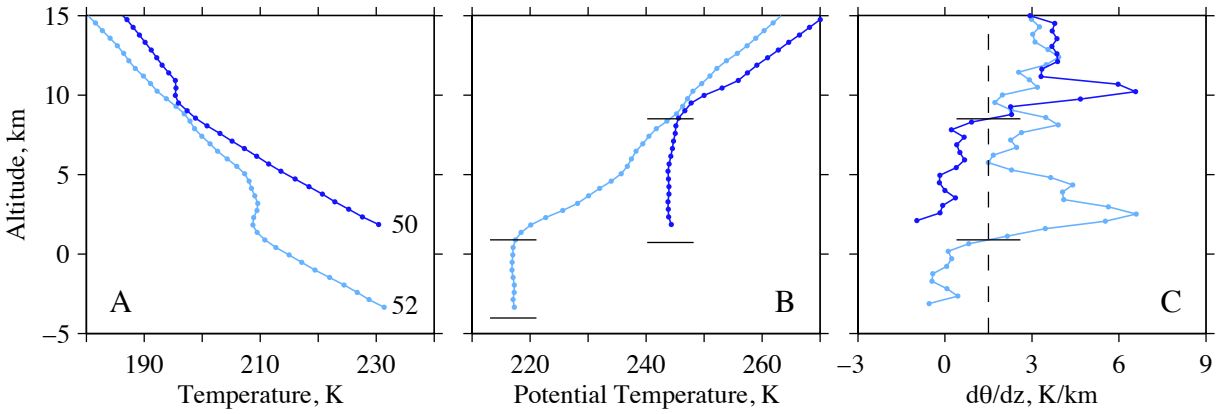

Figure 2: (A) Profiles of T from early spring ($L_s = 16°$) of MY28, one at 273°E, 33°N (dark blue) and the other at 339°E, 33°N (light blue). These profiles correspond to row numbers 50 and 52 of Table 2. The sample spacing is about 500 m. The local time is 15.3 h. The interval between the observations is 0.8 sols. (B) The corresponding profiles of θ. (C) Profiles of $d\theta/dz$ for the same pair of observations. The horizontal lines in (C) indicate the top of the CBL, defined as the level where the dashed vertical line at 1.5 K km^{-1} intersects the profile of $d\theta/dz$. The horizontal lines in (B) indicate the elevation at the top of the CBL and at the surface.

in Acidalia Planitia (4.9 km, 217 K) than for the one in Tempe Terra (7.8 km, 244 K), as shown in Fig. 2B. These differences greatly exceed the uncertainties in θ_m and D (about 0.5 K and 0.3 km, respectively).

The solution for D depends on the resolution of the MOLA map used to specify the surface elevation — all results reported here are from the MOLA map at 0.25° resolution. We characterized this source of uncertainty by comparing MOLA maps with resolutions of 0.25° and 1°. At the 114 locations sampled by RO measurements (Fig. 1), the difference in surface elevation between the two maps has an average value of only 10 m and a standard deviation of about 200 m. The latter is much smaller than both the minimum value and the natural variability of D, as shown below in Fig. 8. Hence, the results and conclusions are essentially the same regardless of which map is used to represent the surface topography.

3.2. Tabulation of results

We applied the method of analysis described in Section 3.1 to the two sets of profiles. The results are summarized in Tables 2 and 3; electronic versions of these tables can be downloaded from Mendeley Data (Hinson, 2018, doi:10.17632/kgvvmgvbnh.1). Only five profiles from MY28 have been published previously (Tellmann et al., 2013; Pätzold et al., 2016); this is the first analysis of the complete set of observations. At the same time, we have re-examined the profiles from MY27, building on results reported in previous publications (Hinson et al., 2008; Spiga et al., 2010a,b).

3.2.1. MY28

We begin with the observations from MY28. Table 2 includes the following information. We use the row number (column 1) as a unique identifier for each observation. Columns 2–4 list the values of L_s, latitude ϕ, and east longitude λ, respectively. Column 5 is the surface elevation z_s from the MOLA map at 0.25° resolution. Column 6 is the daytime surface temperature, as discussed below. The entry in column 7 is θ_s, a measure of surface forcing defined in Section 4.3. Columns 8 and 9 list the solutions for θ_m and D. Column 10 is the local true solar time (LT). The ray path azimuth (column 11) is the direction to MEx at the time and location where the RO ray path grazed the surface of Mars; local north is 0°, east is 90°, and so on.

The CBL forms in response to solar heating of the surface and the resulting large increase of daytime surface temperature; this forcing varies significantly with L_s, ϕ, and λ. We characterized these spatial and seasonal variations using observations by the MGS Thermal Emission Spectrometer (TES), which measured both daytime (14 h) and nighttime (2 h) surface temperatures with complete global coverage for nearly 3 MY (Smith, 2004). Here we consider only the TES observations from the dayside, which are close to the local time of the RO measurements. The TES data were sorted into bins of size 5° in L_s, 3° in ϕ, and 7.5° in λ, with a separate set of bins for each MY in which data are available. The average surface temperature T_s was then computed from all samples within each bin.

TES observations with continuous global coverage ended in late spring of MY27, prior

to the RO observations in Table 2. We therefore used TES measurements from MY27 as an estimate for the surface temperature in MY28. The error associated with this assumption can be assessed by comparing TES measurements of T_s from different years at the same location and L_s. While there are significant differences at high latitudes near the edge of the seasonal CO_2 ice cap, the year-to-year variations in T_s at mid-to-low latitudes are typically less than 2 K at the locations indicated in Fig. 1.

For context, Fig. 3 characterizes the variations of T_s with latitude and longitude at the season of interest. At $L_s = 5°$, the edge of the CO_2 ice cap has receded to about 60°N in a typical year (Benson and James, 2003), poleward of the measurements considered here.

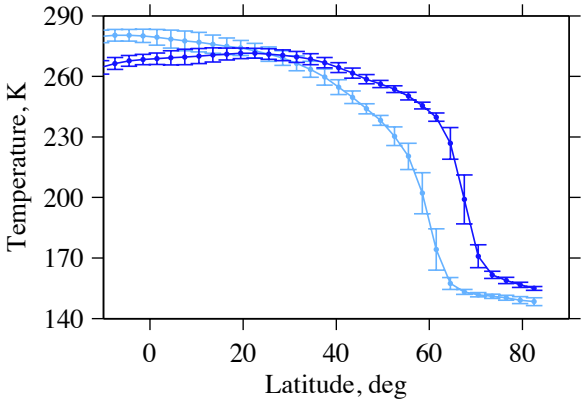

Figure 3: Spatial variations of daytime (14 h) surface temperature as observed by the MGS TES (Smith, 2004). Results are shown for two seasonal windows of MY27, $L_s = 0$–$5°$ (light blue) and 35–40° (dark blue). Dots indicate the zonal average of T_s, with a sample spacing in latitude of 3°. Vertical bars indicate the standard deviation of the zonal variations.

Table 2
Results from RO measurements in late winter of MY27 and spring of MY28.

Row	L_s (°)	ϕ (°)	λ (°E)	z_s (km)	T_s (K)	θ_s (K)	θ_m (K)	D (km)	LT (h)	Azimuth (°)
1	357.1	54.2	221.7	−3.0	223.0	211.3	195.7	2.1	14.0	59.0
2	357.4	53.9	25.7	−3.9	226.5	210.2	181.7	1.7	14.1	59.4
3	358.0	53.4	353.7	−4.8	213.3	192.9	176.4	1.7	14.1	60.1
4	358.7	52.6	223.6	−2.8	230.6	220.3	201.4	2.2	14.2	61.0
5	359.1	52.2	289.5	−3.5	226.6	213.2	198.6	2.1	14.2	61.5
6	359.9	51.3	61.5	−3.6	227.6	212.3	192.6	1.5	14.3	62.5
7	0.1	51.1	323.5	−4.7	217.6	196.4	172.9	2.7	14.3	62.7
8	0.9	50.3	95.3	−4.6	242.6	220.9	187.0	3.1	14.3	63.7
9	1.3	49.8	161.3	−3.8	241.0	226.0	199.3	3.4	14.4	64.2
10	1.5	49.6	63.3	−3.5	237.6	222.5	203.1	1.8	14.4	64.3
11	1.7	49.4	227.2	−2.4	238.4	228.8	209.1	2.7	14.4	64.6
12	1.9	49.2	129.2	−4.7	238.1	215.3	182.8	2.2	14.4	64.8
13	2.1	48.9	293.1	−1.5	236.9	232.6	211.3	2.9	14.4	65.1
14	3.1	47.9	327.0	−4.5	243.2	221.1	183.5	3.0	14.5	66.1
15	3.3	47.7	228.9	−2.0	245.4	237.5	210.8	2.8	14.5	66.2
16	3.4	47.5	130.8	−4.7	242.9	220.3	184.2	2.5	14.5	66.4
17	4.2	46.7	262.6	−0.3	247.9	250.7	220.2	3.4	14.6	67.2
18	4.8	46.1	230.5	−1.7	245.4	238.7	217.0	3.9	14.6	67.8
19	4.9	45.9	132.4	−4.7	242.9	220.7	192.3	2.4	14.6	68.0
20	5.2	45.6	296.3	−1.1	248.0	246.3	218.7	4.4	14.6	68.2
21	5.6	45.1	2.2	−4.2	248.6	229.2	203.9	2.9	14.7	68.6
22	6.3	44.4	232.0	−1.1	257.5	254.2	221.1	5.7	14.7	69.3
23	6.7	43.9	297.8	−1.5	250.9	245.8	210.4	3.3	14.7	69.7
24	6.8	43.7	199.8	−4.0	250.3	231.4	207.3	3.1	14.7	69.8
25	7.8	42.7	233.5	−0.3	255.5	256.8	227.5	4.5	14.8	70.7
26	8.2	42.2	299.3	−1.2	250.9	246.4	217.1	4.5	14.8	71.0
27	8.3	42.0	201.3	−3.9	250.3	231.4	210.1	3.3	14.8	71.2
28	8.5	41.9	103.2	−5.0	251.5	227.7	205.2	3.0	14.8	71.3
29	8.6	41.8	5.2	−3.8	255.5	237.7	204.2	2.9	14.9	71.4
30	8.8	41.7	267.1	+0.5	263.9	271.6	234.3	4.7	14.9	71.5
31	8.9	41.4	169.1	−3.8	256.1	238.1	203.2	2.9	14.9	71.7
32	9.0	41.3	71.0	−3.1	255.7	241.6	215.1	3.0	14.9	71.8

Table 2 (continued)
Results from RO measurements in late winter of MY27 and spring of MY28.

Row	L_s (°)	ϕ (°)	λ (°E)	z_s (km)	T_s (K)	θ_s (K)	θ_m (K)	D (km)	LT (h)	Azimuth (°)
33	9.6	40.7	38.8	−1.6	256.5	250.9	222.4	5.0	14.9	72.2
34	9.7	40.5	300.6	−1.2	254.7	251.1	221.4	3.7	14.9	72.3
35	9.8	40.3	202.7	−3.9	255.5	236.3	205.2	2.6	14.9	72.5
36	10.0	40.2	104.5	−5.0	251.5	227.0	203.4	3.7	14.9	72.6
37	10.4	39.7	170.4	−3.9	258.5	240.4	213.1	2.9	15.0	72.9
38	10.7	39.4	334.2	−4.5	257.4	235.5	208.3	3.7	15.0	73.2
39	10.9	39.1	138.1	−4.3	253.4	232.8	206.4	3.4	15.0	73.4
40	11.1	39.0	40.0	−0.9	260.3	257.7	225.0	4.9	15.0	73.5
41	11.2	38.8	301.9	−1.7	258.8	252.6	225.8	5.5	15.0	73.6
42	11.9	38.0	171.6	−3.9	262.9	244.1	216.1	3.9	15.0	74.2
43	12.1	37.7	335.5	−4.4	261.0	239.6	211.8	4.6	15.0	74.4
44	12.4	37.4	139.3	−4.2	258.4	238.0	212.0	3.7	15.1	74.6
45	13.5	36.2	74.7	−2.6	258.0	246.0	219.1	3.7	15.1	75.4
46	13.6	36.0	336.6	−4.3	261.0	240.7	220.0	5.4	15.1	75.5
47	14.0	35.6	42.3	−0.0	267.9	270.9	234.8	6.2	15.1	75.8
48	15.0	34.5	75.8	−2.6	260.0	247.6	224.3	3.5	15.2	76.5
49	15.5	33.9	43.4	−0.2	266.8	268.5	234.7	5.9	15.2	76.9
50	16.2	33.2	272.9	+0.7	270.5	280.1	244.2	7.8	15.2	77.4
51	16.4	32.8	76.8	−2.4	262.4	251.3	222.8	3.5	15.3	77.6
52	16.6	32.6	338.7	−4.0	267.9	248.1	217.1	4.9	15.3	77.7
53	17.0	32.2	44.4	−0.9	268.7	266.8	234.9	6.3	15.3	78.0
54	17.1	32.0	306.2	−3.1	265.9	250.3	218.0	3.8	15.3	78.1
55	17.9	31.1	77.7	−1.6	262.4	255.1	227.2	4.1	15.3	78.7
56	18.1	30.9	241.5	+2.0	271.4	287.7	243.1	6.7	15.3	78.8
57	21.4	26.9	309.0	−3.7	272.0	254.1	222.3	5.7	15.5	81.1
58	21.6	26.8	210.9	−3.4	275.0	257.2	219.6	4.9	15.5	81.2
59	23.0	25.1	211.8	−3.0	275.0	259.9	221.7	5.7	15.5	82.1
60	23.9	24.2	245.0	+2.4	274.8	293.2	248.3	7.4	15.6	82.7
61	24.5	23.5	212.7	−3.1	275.4	260.1	223.0	5.8	15.6	83.0
62	25.1	22.7	82.1	−2.2	267.9	258.0	224.9	4.5	15.6	83.5
63	25.2	22.6	344.0	−1.9	273.0	264.9	231.6	8.3	15.6	83.5
64	26.3	21.4	279.1	−0.1	274.1	277.0	237.3	5.6	15.6	84.2

Table 2 (continued)
Results from RO measurements in late winter of MY27 and spring of MY28.

Row	L_s (°)	ϕ (°)	λ (°E)	z_s (km)	T_s (K)	θ_s (K)	θ_m (K)	D (km)	LT (h)	Azimuth (°)
65	26.5	21.0	83.0	−2.9	267.9	253.7	223.2	4.3	15.6	84.4
66	26.8	20.9	246.8	+2.5	274.6	294.0	251.7	8.6	15.7	84.5
67	28.6	18.4	313.3	−3.5	269.4	252.6	222.2	5.2	15.7	85.6
68	29.2	17.6	182.8	−3.3	276.1	259.8	224.3	7.2	15.7	86.0
69	29.4	17.4	84.7	−3.7	268.0	249.4	219.4	4.0	15.7	86.1
70	29.5	17.4	346.6	−1.7	273.2	267.7	232.3	6.6	15.7	86.2
71	30.1	16.6	216.1	−2.2	273.9	263.6	227.8	5.5	15.8	86.6
72	30.3	16.3	117.9	−3.2	268.0	252.5	225.8	5.5	15.7	86.6
73	32.1	14.1	184.4	−3.2	274.9	258.9	226.1	7.3	15.8	87.7
74	32.2	13.9	86.3	−3.8	267.7	248.0	219.8	4.1	15.8	87.8
75	34.1	11.6	54.7	+1.4	273.3	284.4	247.6	9.7	15.8	88.9
76	38.4	4.8	318.7	−1.3	264.4	260.0	233.0	6.0	15.9	91.4
77	38.8	4.3	24.4	+0.2	274.4	279.4	240.8	5.8	15.9	91.6
78	38.9	4.1	286.2	+1.4	268.4	281.0	241.3	4.1	15.9	91.7
79	39.0	3.5	188.1	−3.2	271.4	256.4	223.3	5.1	15.9	91.8
80	40.4	0.9	188.7	−2.9	268.5	254.1	222.6	4.8	15.9	92.6
81	40.6	0.9	90.6	−0.4	263.3	262.9	229.9	3.0	15.9	92.7
82	42.3	−3.6	156.5	−2.3	261.6	251.1	226.2	5.1	15.9	93.7

3.2.2. MY27

Table 3 summarizes the results from MY27. Contemporaneous TES measurements of T_s are available for this set of observations. The definition for the top of the CBL is slightly different than the one used in previous analysis of these profiles (Hinson et al., 2008); the resulting change in D is typically smaller than the measurement uncertainty of about 0.3 km. Table 3 also contains several useful parameters (z_s, T_s, θ_s, and θ_m) that were not published previously.

Table 3
Results from RO measurements in midspring of MY27.

Row	L_s (°)	ϕ (°)	λ (°E)	z_s (km)	T_s (K)	θ_s (K)	θ_m (K)	D (km)	LT (h)	Azimuth (°)
1	44.5	27.5	107.0	−4.3	264.4	241.6	214.0	4.6	17.1	102.3
2	45.9	24.4	106.9	−3.9	265.5	244.8	217.8	5.5	17.1	102.8
3	47.1	21.8	205.0	−3.9	272.6	251.2	218.6	5.2	17.2	103.3
4	47.8	20.6	74.0	+0.2	270.9	272.6	238.0	9.4	17.2	103.6
5	48.4	19.3	303.0	−0.9	268.2	266.0	232.5	7.7	17.2	103.8
6	48.8	18.6	8.4	−1.6	271.2	264.4	234.2	8.4	17.2	104.0
7	49.0	18.0	172.0	−2.2	266.9	254.8	224.2	6.9	17.2	104.1
8	49.1	17.8	73.8	−0.5	272.1	270.0	237.4	9.2	17.2	104.1
9	49.2	17.5	335.6	−2.9	264.5	250.0	226.7	6.2	17.2	104.2
10	49.4	17.4	237.5	+0.9	272.0	278.7	242.2	7.9	17.2	104.2
11	51.2	13.7	204.6	−3.6	268.6	249.5	219.4	4.3	17.2	105.0
12	51.5	13.3	8.2	−1.5	270.0	264.1	233.8	7.0	17.2	105.1
13	51.6	13.3	270.0	+1.9	267.8	279.5	247.0	8.7	17.2	105.2
14	52.1	12.3	237.2	+2.5	270.1	287.1	244.6	8.0	17.2	105.4
15	53.2	10.3	73.5	+1.0	274.1	281.1	245.6	11.5	17.1	105.9
16	53.3	10.0	335.3	−3.1	261.0	246.2	225.6	6.3	17.1	105.9
17	53.7	9.5	40.7	+0.6	270.7	276.9	239.3	7.6	17.1	106.1
18	53.8	9.2	302.5	−0.6	261.4	261.7	238.3	8.8	17.1	106.1
19	54.1	8.8	106.1	−0.7	260.5	258.8	232.7	8.9	17.1	106.2
20	54.3	8.4	269.8	+1.8	265.5	279.6	248.6	9.4	17.1	106.3
21	57.4	3.3	335.0	−2.8	260.3	247.3	225.9	6.0	17.1	107.7
22	58.5	1.5	171.3	−3.0	264.0	249.6	220.7	5.4	17.1	108.2
23	58.6	1.5	73.1	+1.5	269.0	279.2	246.1	9.5	17.1	108.3
24	60.8	−1.9	105.7	+0.3	257.1	261.3	231.9	3.6	17.1	109.3
25	61.3	−2.5	73.0	+1.9	267.4	280.2	242.4	8.3	17.1	109.5
26	62.2	−3.9	105.6	+0.1	259.1	262.0	232.6	5.1	17.1	109.9
27	63.9	−6.4	171.0	−2.9	254.2	241.2	216.8	3.9	17.1	110.7
28	64.8	−7.6	203.8	−1.1	257.3	253.6	226.3	5.5	17.1	111.1
29	65.2	−8.3	171.0	−2.8	252.8	240.1	217.7	4.9	17.1	111.3
30	66.5	−9.7	269.2	+4.3	250.9	280.2	251.3	9.0	17.0	111.9
31	67.9	−12.1	170.7	−1.8	245.2	238.8	215.8	3.0	17.0	112.6
32	69.2	−13.5	268.9	+5.4	247.1	283.4	248.7	6.5	17.0	113.2

4. Selected RO results

This section addresses four topics. First, we illustrate the typical appearance of the RO profiles and the general properties of the CBL. Second, we identify the signature of fronts in midlatitude measurements from MY28. Third, we characterize the response of the CBL to spatial variations in surface forcing. Finally, we take an initial look at several atypical profiles in preparation for the Isidis regional study (Section 6).

4.1. Typical profiles

4.1.1. MY28

As an introduction to the measurements from MY28, Fig. 4 shows four profiles at 47–50°N, near the northern limit of the latitude coverage. The local time is 14.5 h. Two of the profiles are from Utopia Planitia and the second pair is from a location northwest of Alba Patera, where the surface elevation is 2.5 km higher. Successive measurements at each location are essentially the same. In early spring at this latitude, the mixed layer is relatively shallow, about 2.4 km in Utopia and 2.8 km northwest of Alba Patera; θ_m is 26 K colder in Utopia.

Fig. 5 shows a group of profiles from midspring at 1-5°N, near the southern limit of the latitude coverage in MY28. The local time is 15.9 h. As in Fig. 4, there is little variation between successive measurements at nearly the same location (Lucus Planum in this case). The profiles sample a range of surface elevations, and θ_m increases from 223 K in Lucus Planum (lowest elevation) to 241 K in Terra Sabaea (highest elevation). The depth of the CBL ranges from 4.8 to 6.0 km.

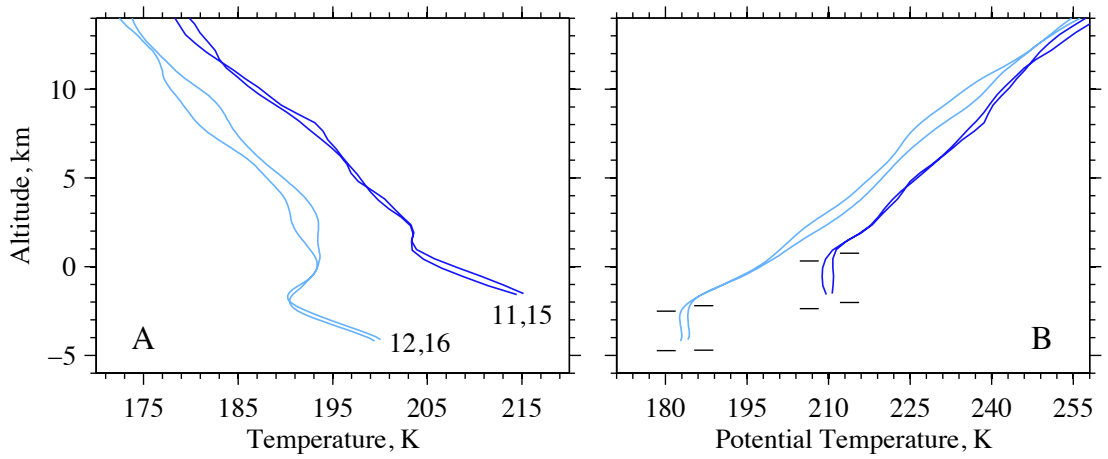

Figure 4: (A) Profiles of T at northern midlatitudes near $L_s = 3°$ of MY28. Each profile is labeled with the row number of the corresponding entry in Table 2. The colder pair (light blue) is from Utopia Planitia (130°E, 48°N) and the warmer pair (dark blue) is from a location northwest of Alba Patera (228°E, 49°N). The interval between the two observations at each location is 3 sols. (B) The corresponding profiles of θ. Horizontal lines adjacent to each profile indicate the elevation at the surface and at the top of the CBL. The 1-sigma uncertainty in potential temperature increases from about 0.3 K at the base of each profile to about 0.7 K at 10 km altitude.

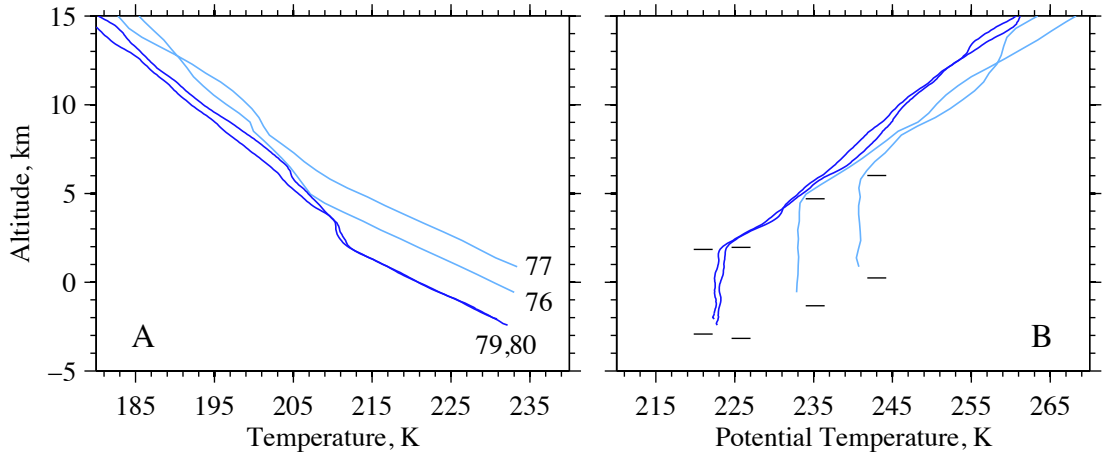

Figure 5: Equatorial profiles of (A) T and (B) θ from a 5-sol span near $L_s = 39°$ of MY28. Moving from lowest to highest surface elevation, profiles 79 and 80 are from nearly the same location in Lucus Planum (188°E, 2°N), profile 76 is from Xanthe Terra (319°E, 5°N), and profile 77 is from Terra Sabaea (24°E, 4°N). The interval between the pair of observations in Lucus Planum is 3 sols. See Fig. 4 for further discussion.

4.1.2. MY27

The profiles from MY27 are similar in character to those from MY28, as shown in Fig. 6. These four profiles are spaced uniformly across a 100° span of longitude centered on Chryse Planitia. Conditions range from θ_m = 226 K and D = 6.0 km for profile 21 near Tiu Vallis to θ_m = 249 K and D = 9.4 km for profile 20 on the Tharsis Plateau. Within this group of observations, both θ_m and D grow steadily with increasing surface elevation. (We return to this topic in Section 4.3.) At the local time of these observations (17.1 h), daytime convection has ended, as reflected by the marginally stable stratification within the residual CBL. Nonetheless, the top of the CBL is still marked by a distinctive change in static stability. There is an unusually large gap between the base of profile 21 and the surface, where local topography prevents limb sounding of the lowest few kilometers of the atmosphere.

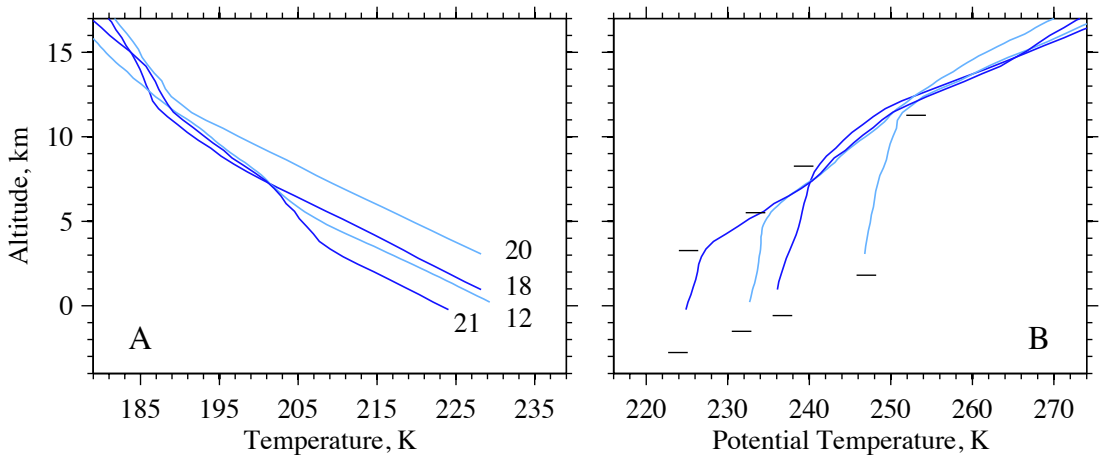

Figure 6: Profiles of (A) T and (B) θ at L_s = 52°–57° of MY27. Profile 20 is from the Tharsis Plateau (270°E, 8°N), profile 18 is from Xanthe Terra (303°E, 9°N), profile 21 is near Tiu Vallis (335°E, 3°N), and profile 12 is from southern Arabia Terra (8°E, 13°N). See Fig. 4 for further discussion.

4.2. Fronts

Baroclinic instability at the edge of the CO_2 ice cap generates shallow, planetary-scale, traveling waves at mid-to-high latitudes in early northern spring (Lewis et al., 2016, Figs. 1 and 2). This type of weather system appears to be responsible for occasional day-to-day variability in the midlatitude RO profiles from MY28.

Fig. 7 shows the possible signature of a cold front in a sequence of three profiles from nearly the same location in Tempe Terra. The interval between successive observations is 3 sols. The first and third profiles are essentially the same but both differ significantly from the second profile, which is 8 K colder within the CBL and 4 K warmer in the lowest 4 km of the overlying free air. We interpret this as the signature of a cold front that passed through Tempe Terra between the first and second observations; roughly 3 sols later the temperature structure had returned to its unperturbed state. This interpretation is consistent with results reported by Wang et al. (2005, Fig. 6), where a surge of cold, dense air was observed behind a southward-moving frontal dust storm in Acidalia.

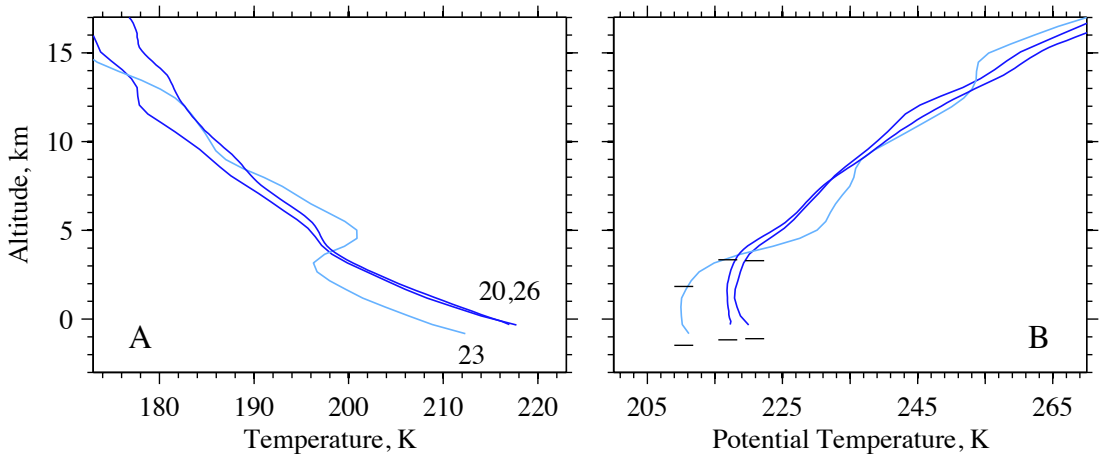

Figure 7: Sol-to-sol variations of (A) T and (B) θ in Tempe Terra in early spring of MY28 ($L_s = 7°$). The three profiles correspond to row numbers 20, 23, and 26 of Table 2. The interval between successive observations is 3 sols; the location of all three profiles is about the same (298°E, 44°N). Profile 23 (light blue) differs markedly from the other two (dark blue) within 9 km of the surface. See Fig. 4 for further discussion.

Several other profiles from MY28 show similar signs of frontal activity. The most reliable results come from sequences of three or more profiles obtained as quickly as possible at nearly the same location, as in Fig. 7. In addition to the example in Fig. 7, events that can be identified with confidence include a cold front in western Arcadia Planitia at $L_s = 9°$ (row 31 of Table 2; rows 37 and 42 complete the sequence) and a warm front in Acidalia Planitia at $L_s = 14°$ (row 46 of Table 2; rows 38, 43, and 52 complete the sequence). These early spring weather systems have a significant impact on conditions near the surface, changing the temperature by as much as 10 K and the density by up to 5%, but they do not appear to reach the tropics.

4.3. Response to surface forcing

The RO observations sampled basic properties of the CBL across a wide range of surface conditions (z_s and T_s), as summarized in Tables 2 and 3. These measurements reveal distinctive patterns of behavior, which can be used to evaluate the performance of numerical models (see Section 6.1). In this section we focus on the response of θ_m and D to variations in surface forcing θ_s, defined by analogy with Eq. (1):

$$\theta_s = T_s \, (p_o/p_s)^{R/c_p} \, . \tag{2}$$

The surface forcing is proportional to T_s and becomes more intense at high elevation, where the surface pressure p_s is small. This dependence on p_s is known as the pressure effect (Spiga et al., 2010a,b).

The sensitivity of θ_s to changes in T_s and p_s can be determined by differentiating Eq. (2):

$$d\theta_s/\theta_s \approx T_s^{-1} \, (dT_s + dz_s \, g/c_p) \, , \tag{3}$$

where g is the acceleration of gravity, and we have converted the change in surface pressure dp_s to a change in surface elevation dz_s. In the lower atmosphere of Mars, g/c_p is about 5 K/km; a 1-km change in z_s is therefore equivalent to a 5-K change in T_s.

Eq. (2) requires an estimate for p_s, which was obtained by extrapolating the pressure at the base of the RO profile to the local surface elevation z_s. We then combined p_s with the TES measurement of T_s to compute θ_s. The results appear in Tables 2 and 3.

The diurnal cycle of θ_s is determined primarily by variations in T_s; the effect of diurnal variations in p_s is insignificant. Hence, the local time for the measurements of θ_s is 14 h, when TES observed the dayside. This is a few hours earlier than the local time when θ_m was measured, 17 h in MY27 and 15–16 h in MY28. At these local times, both θ_s and θ_m are near their respective peak values in the diurnal cycle (see Section 5.3), which simplifies the interpretation of the measurements.

For the observations in both MY27 and MY28, there is a clear correlation between the surface forcing and the properties of the CBL, as shown in Fig. 8. We characterized the response of θ_m and D to variations in θ_s through least-squares linear fits (Brandt, 1989, Section 9-2). The potential temperature of the mixed layer is modeled as

$$\theta_m = \alpha\,\theta_s + \beta\,, \tag{4}$$

where α is the slope and β is the intercept. An analogous model is used for D, with slope γ and intercept δ. The results appear in Fig. 8 and Table 4.

Table 4
Linear fits to θ_m and D.

MY	α (K/K)	β (K)	γ (km/K)	δ (km)
27	0.72 ± 0.04	43.7 ± 9.8	0.11 ± 0.02	-20.7 ± 4.2
28	0.71 ± 0.03	41.4 ± 6.5	0.08 ± 0.01	-14.4 ± 2.1

Note: All uncertainties are one sigma.

Eq. (4) provides a good fit to the data in Figs. 8A and 8C. In both MY27 and MY28, the difference between the measurements of θ_m and the linear fit has a standard deviation of 3.1 K, much smaller than the natural variability of both θ_m and θ_s. However, the residuals exceed the formal uncertainty of the measurements and are the dominant source of noise in the linear fit. In deriving error bars on the solutions for α and β, we therefore assigned a one-sigma uncertainty of 3.1 K to each measurement of θ_m, assumed the errors to be independent, and treated the samples of θ_s as error free. Table 4 lists the resulting one-sigma uncertainties in α and β. We used the same approach in assigning error bars to the estimates of γ and δ.

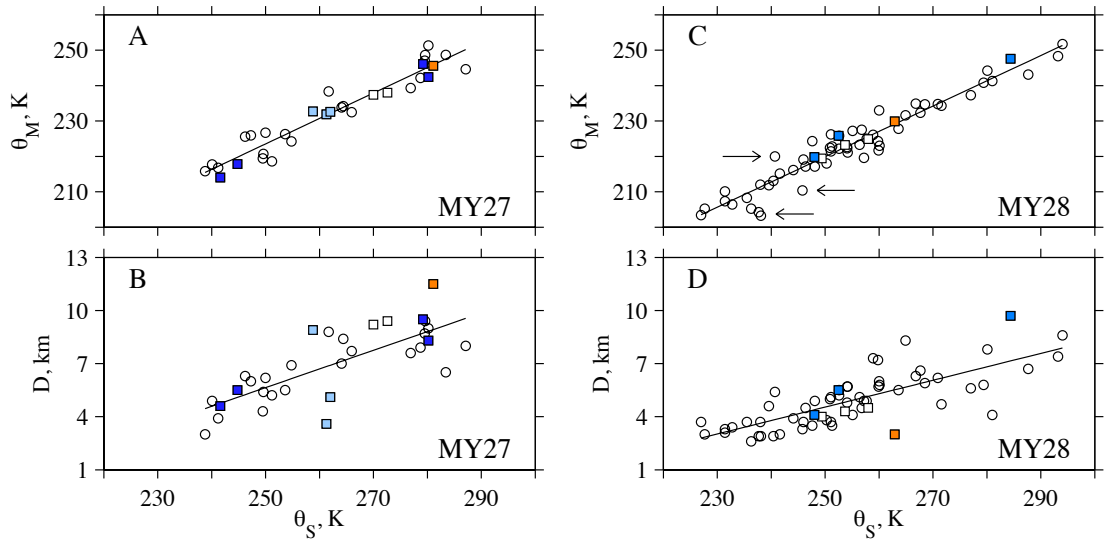

Figure 8: Response of (top row) θ_m and (bottom row) D to variations in θ_s at fixed local time. Panels (A) and (B) show RO measurements at 28°N–14°S in late spring (L_s = 44–70°) of MY27. Panels (C) and (D) show RO measurements at 45°N–4°S in early spring (L_s = 6–43°) of MY28. Each panel includes a least-squares linear fit (Table 4). Squares denote measurements used in the Isidis regional study (Section 6), with colors to facilitate subsequent discussion. All other measurements are denoted by circles. The arrows in (C) indicate measurements affected by fronts, which cause transient cooling or warming of θ_m.

The measurements in MY28 sampled a large range of θ_s, from a minimum of 227 K in Utopia Planitia (row 36 of Table 2) to a maximum of 294 K on the Tharsis Plateau (row 66 of Table 2). This 67-K increase in θ_s results from the combined effects of a 7.5-km increase in z_s and a 23-K increase in T_s. The samples of θ_m at these two locations lie at the endpoints of the linear fit in Fig. 8C.

The solutions for α and β are essentially the same in MY27 and MY28. This suggests that the linear dependence of θ_m on θ_s is a fundamental property of the CBL, as least in northern spring at mid-to-low latitudes. On average θ_s is about 30 K warmer than θ_m; the solution for α shows that the size of the offset depends on the surface forcing, increasing by about 3 K for each 10 K increase in θ_s.

In measurements at northern midlatitudes in MY28, θ_m is influenced not only by variations in θ_s but also by advection. Several profiles were perturbed by fronts, as discussed

in Section 4.2. The corresponding samples of θ_m — identified by arrows in Fig. 8C — deviate noticeably from the linear fit. (It is unclear what causes other outliers of similar magnitude in Fig. 8C.) In addition, all profiles at latitudes poleward of 45°N appear to be strongly affected by large-amplitude stationary waves. Fig. 4 shows an example; the temperature structure varies markedly with longitude, but the sol-to-sol variation at each location is comparatively small. The change in θ_s between the two locations, about 15 K, is 40% smaller than the change in θ_m, about 26 K. In this case the impact of advection is so large that it obscures the response of θ_m to surface forcing. For this reason, we have excluded measurements poleward of 45°N from Fig. 8 (rows 1–21 of Table 2).

In general, stronger surface forcing produces a deeper CBL, as shown in Figs. 8B and 8D. The range of D is about the same in both years, 3.0–11.5 km in MY27 and 2.6–9.7 km in MY28. Linear fits to the data have slopes of 0.11 ± 0.02 km/K in MY27 and 0.08 ± 0.01 km/K in MY28, so that a 10-K increase in θ_s results in a 1-km increase in D. The slope is smaller in MY28 than MY27, but the difference is comparable to the uncertainties and may not be significant.

Several samples of D differ considerably from the linear fits in Figs. 8B and 8D. As there is nothing unusual about the corresponding values of θ_m, this strong modulation in the depth of the mixed layer does not appear to be a direct response to surface forcing. In both MY27 and MY28, there are four outliers where the deviation of D from the linear fit exceeds 2 km. Five of these eight cases are in the general vicinity of Isidis Planitia. We take a close look at this region in Sections 5 and 6, which show that D is influenced by the topographic circulation near the rim of Isidis.

4.4. Isidis Planitia and its surroundings

There are significant differences between contemporaneous profiles in Isidis and Amazonis, as shown in Fig. 9. The latitude and local time are essentially the same for all four profiles, and the sol-to-sol variations are relatively small in both topographic basins. However, the surface forcing is stronger in Amazonis, where θ_s is nearly 11 K larger owing to an 8-K increase in T_s and a 0.5-km increase in z_s. In response to this change in θ_s, θ_m increases

by about 6 K. There is also a large change in D, from about 4 km in Isidis to more than 7 km in Amazonis.

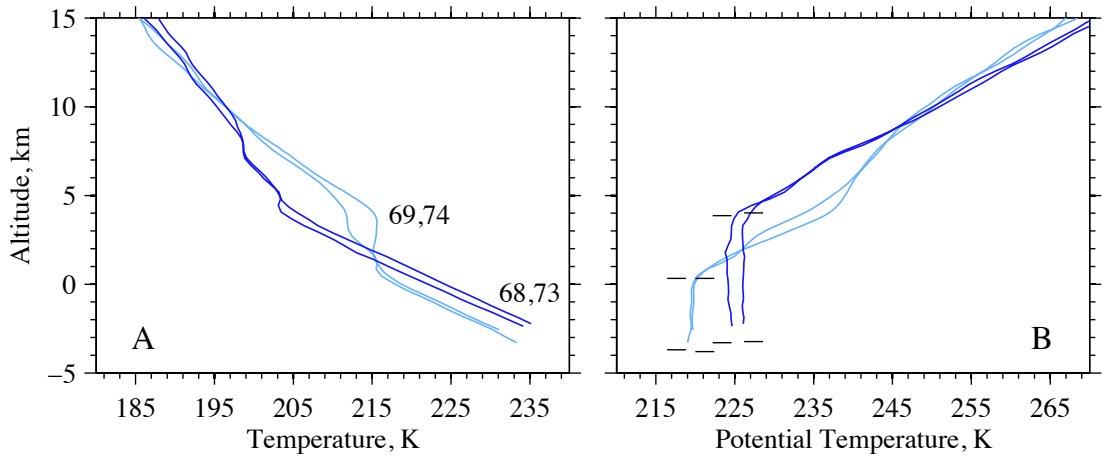

Figure 9: (A) Profiles of T in the northern tropics from a 6-sol span at $L_s \approx 31°$ in MY28 and (B) the corresponding profiles of θ. Profiles 68 and 73 (dark blue) are from Amazonis (184°E, 16°N); profiles 69 and 74 (light blue) are from Isidis (86°E, 16°N). The local time is 15.8 h. See Fig. 4 for further discussion.

The vertical structure above the mixed layer is more intriguing. Although the four profiles in Fig. 9 agree closely at altitudes above 9 km, the free air at lower altitudes is much warmer in Isidis, by about 9 K at 4 km altitude. This warm layer in the Isidis profiles may be a consequence of low altitude subsidence and adiabatic warming within the Isidis basin. We return to this topic in Section 6.2.

Fig. 10 shows two profiles from the rim of Isidis where D deviates from the general trend in Figs. 8B and 8D. In profile 15 of MY27, θ is nearly constant at altitudes of 6–12 km, suggesting that the CBL extended upward into this altitude range at an earlier time of day. This interpretation implies that the CBL is exceptionally deep at this location, 11.5 km, as indicated by the orange square in Fig. 8B. But at the time of this observation (17.1 h), the lower part of profile 15 has cooled significantly, by as much as 8 K adjacent to the surface, resulting in stable stratification at altitudes below 6 km. This type of structure is atypical of the late-afternoon CBL.

Fig. 10 implies that conditions are quite different on the southern rim of Isidis. Profile 81

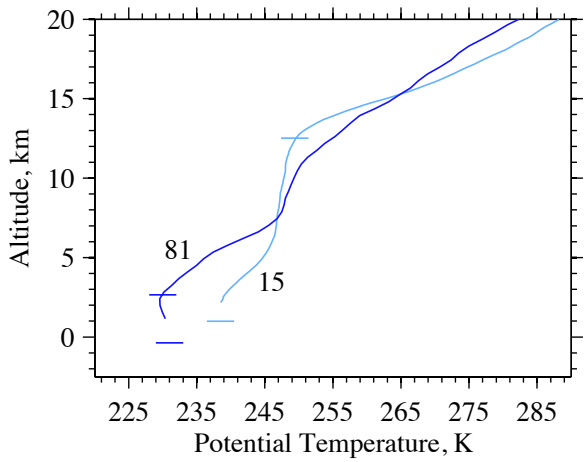

Figure 10: Profiles of θ from the rim of Isidis. Profile 15 of MY27 (light blue) is from the western rim (73.5°E, 10.3°N), where the CBL is exceptionally deep. Profile 81 of MY28 (dark blue) is from the southern rim (90.6°E, 0.9°N), where the CBL is unusually shallow. The local time is 17.1 h for profile 15 and 15.9 h for profile 81. See Fig. 4 for further discussion.

of MY28 has an unusually shallow mixed layer, with a depth of only 3.0 km, as indicated by the orange square in Fig. 8D. In Section 6.2 we test the performance of a mesoscale model through detailed comparisons with the anomalous profiles in Fig. 10.

5. The OSU Mars Mesoscale Model

Like many Martian atmospheric models, the OSU Mars Mesoscale Model (MMM) has terrestrial heritage, in this case the fifth-generation Penn State/NCAR Mesoscale Model; Tyler et al. (2002) explain its adaptation to Mars. The subsequent development and application of the model are described by Tyler and Barnes (2005, 2013, 2015) and Tyler et al. (2008). This section discusses the configuration of the model and introduces the simulation used in this study.

5.1. General description

The MMM comprises a semi-global polar stereographic mother domain and a set of embedded, high-resolution nests. The mother domain is initialized by the NASA/Ames

Mars General Circulation Model (MGCM) (Haberle et al., 1999), which also provides hourly updates to boundary conditions. Use of a polar stereographic mother domain along with a carefully designed interface between the models ensures that information passes smoothly from the MGCM to the MMM (Tyler et al., 2002). In addition, the models use the same radiation code and consistent representations of surface properties.

The objectives of this investigation can be achieved by running the model with the mother domain and a single nest centered on Isidis Planitia. The horizontal resolution, which varies with location, is typically 108 km in the mother domain and 36 km in the nest. The MMM uses sigma vertical coordinates, implemented here with 55 levels ranging from about 7 m above the surface to 80 km altitude (0.02 Pa). The level spacing decreases from 5.7 km at the top of the model to 17 m near the surface, with 24 levels in the lowest 10 km above the ground.

A simulation that covers a broad range of L_s is beyond the scope of this investigation. We opted instead for a short simulation consisting of 14 sols for spin up and an additional 6 sols for analysis. The last 6 sols are centered on $L_s = 40°$, near the midpoint of the RO observations considered in Section 6 (L_s = 25–41° of MY28 and L_s = 45–62° of MY27). Within the 36-km nest, sol-to-sol changes in vertical structure at fixed location and local time are negligible (not shown). Hence, the relatively short duration of the simulation does not appear to be a problem. All results reported here are 6-sol averages.

In this simulation the atmosphere is dry and the dynamics are hydrostatic. Both the MGCM and the MMM used a model for atmospheric dust opacity derived from spacecraft observations at $L_s = 40°$ (Smith, 2004; McCleese et al., 2010). Maps of surface properties were constructed from MOLA observations of topography (Smith et al., 2001) and TES observations of albedo (Christensen et al., 2001) and thermal inertia (Putzig et al., 2005).

The convective motion in the daytime mixed layer is not resolved by the 36-km nest. This and other sub-grid-scale processes in the boundary layer are parameterized by the MMM, using the approach described by Hong and Pan (1996) with changes to basic constants as required for application to Mars (Tyler et al., 2002).

5.2. The mother domain

Fig. 11 shows a color-coded map of CBL depth from the mother domain at a local time of 15 h, which illustrates several aspects of the simulation. There are wide variations of D at mid-to-low latitudes, from a minimum of a few kilometers in Valles Marineris and Hellas Planitia to a maximum of more than 12 km above the large volcanoes. In general, the CBL is deeper where the surface elevation is high. Fig. 11 also shows the boundary of the 36-km nest. We take a closer look at this region in the next section.

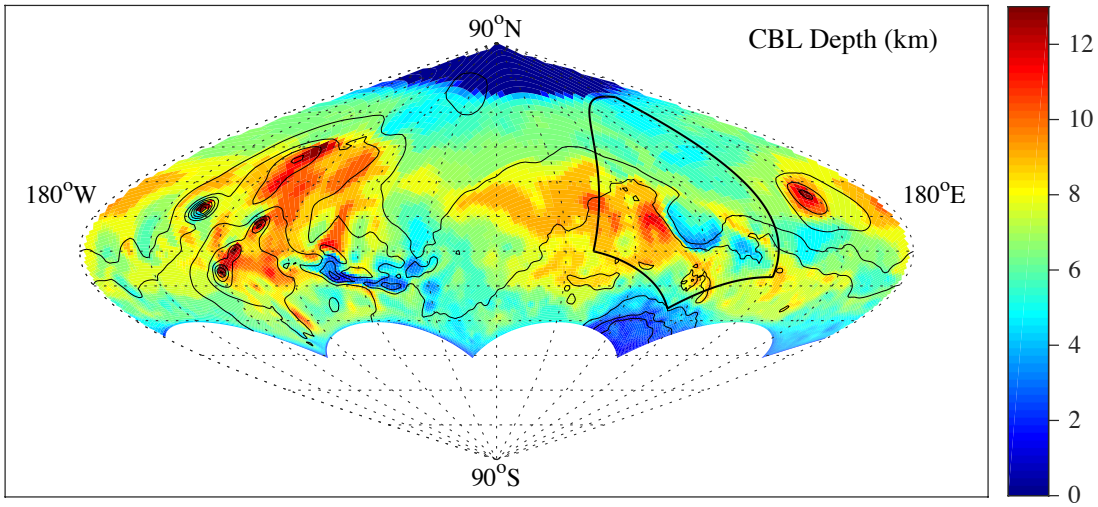

Figure 11: Semi-global map of CBL depth from the mother domain, which covers all locations north of the scalloped border at 30–45°S. Results are shown at a fixed local time of 15 h. At the season of this simulation ($L_s = 40°$), the sub-solar latitude is 16°N. The boundary of the 36-km nest is marked by a thick black line. Contours of surface elevation are indicated by thin black lines at intervals of 2.5 km.

5.3. The 36-km nest

With its threefold enhancement in horizontal resolution, the 36-km nest brings the spatial variations in CBL structure into sharper focus, as shown in Fig. 12. The CBL depth varies dramatically on horizontal scales of only a few hundred kilometers, from a minimum of 2.2 km in southern Isidis Planitia to a maximum of 11.6 km above Syrtis Major. Within Isidis, the CBL is shallowest along an arc adjacent to the steepest surrounding topography. This

result is reminiscent of previous numerical simulations of the circulation in more compact craters, where daytime subsidence produces a capping inversion that restricts the depth of the CBL (Toigo and Richardson, 2003; Tyler and Barnes, 2013, 2015). We return to this topic in Section 6.2, which examines characteristics of the topographic circulation associated with Isidis.

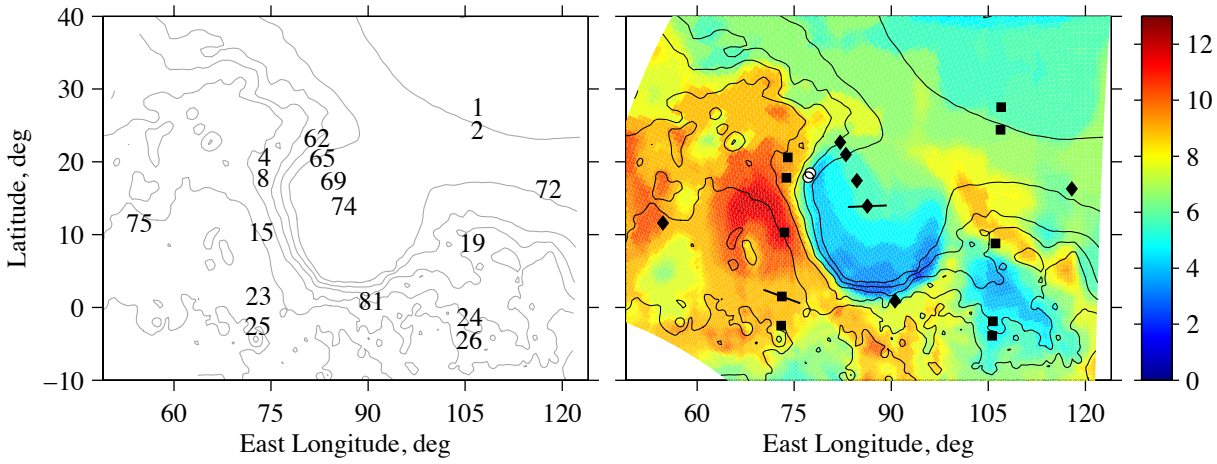

Figure 12: Context for the Isidis regional study in Section 6. Contours of surface elevation are shown at 1-km intervals by (left) gray lines and (right) black lines. A color-coded map of CBL depth (in km) from the 36-km nest appears in the right-hand panel; the local time is 15 h and $L_s = 40°$. Locations of RO observations are indicated by (left) profile numbers and (right) black symbols, with squares and diamonds denoting measurements from MY27 and MY28, respectively. One symbol from each MY includes a line whose length and orientation show the horizontal resolution along the limb-sounding line of sight. White circles (right) mark the locations of two possible landing sites for Mars 2020 (JEZ and NES).

Fig. 12 also shows the locations of 17 RO profiles that fall within this section of the nest. The longitude coverage is improved by combining the observations from MY27 and MY28, which sample a range of conditions in the Isidis basin and its surroundings. In Section 6.1, we assess the performance of the MMM through detailed comparisons between measured and simulated profiles of θ at these 17 locations.

Before proceeding with the Isidis regional study, it is useful to place the RO observations (at fixed local time) into context with the daytime evolution of the CBL. Figs. 13 and 14

show results from the 36-km nest at the location of RO profile 72 (118°E, 16°N), a site in Elysium Planitia where the local topography is relatively flat (Fig. 12). There is nothing unusual about the measured and simulated properties of the CBL at this location.

The energy budget of the surface is controlled largely by absorption of sunlight and emission of infrared radiation (Savijärvi, 1999). Fig. 13 shows the resulting diurnal cycle of surface forcing; θ_s increases dramatically from a minimum of about 170 K at sunrise (5.7 h) to a maximum of 251 K at 13–14 h, followed by a rapid decrease to about 210 K at sunset (18.3 h).

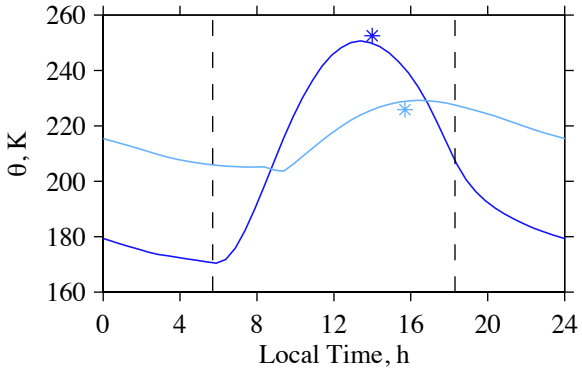

Figure 13: The simulated diurnal cycle of potential temperature from the 36-km nest at 118°E, 16°N (coincident with RO profile 72 of MY28). The two curves show (light blue) θ_{44} and (dark blue) θ_s. The former is the potential temperature at about 1 km above ground level (AGL). Dashed vertical lines indicate the local times of sunrise and sunset. The asterisks show the measurements of (light blue) θ at 1 km AGL and (dark blue) θ_s at the same location.

Fig. 14 shows how profiles of θ evolve in response to the diurnal cycle of surface forcing. During daytime, the profiles contain a thin, highly super-adiabatic layer adjacent to the ground (Fig. 14A), in which the atmosphere is strongly heated by the surface (Haberle et al., 1993; Savijärvi, 1999). The heating results in part from absorption of upwelling infrared radiation, but the sensible heat flux from the ground is also significant, as illustrated in large eddy simulations by Tyler et al. (2008). The temperature structure within this region, known as the surface layer, has been measured by Mars Pathfinder (Schofield et al., 1997) and the Mars Exploration Rovers (Smith et al., 2004, 2006).

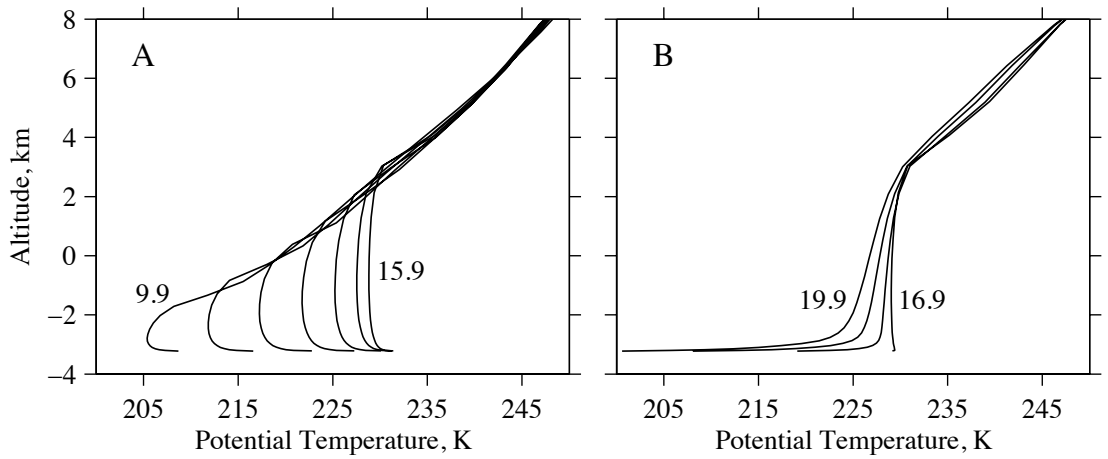

Figure 14: Simulated profiles of θ from the 36-km nest at 118°E, 16°N (coincident with RO profile 72 of MY28). Results are shown at 1-h intervals for local times of (A) 9.9–15.9 h and (B) 16.9–19.9 h. The surface elevation at this location is −3.2 km.

The buoyancy of the surface layer triggers convective mixing at higher altitudes. A mixed layer appears shortly after sunrise and θ_m increases steadily until late afternoon (Fig. 14A). As θ_m increases, convection erodes more deeply into the overlying free air and D grows accordingly, reaching its maximum depth at about the local time of the RO measurements. After sunset, the profile of θ relaxes gradually into stable stratification within the altitude range previously occupied by the CBL, and a strong, shallow temperature inversion develops adjacent to the surface (Fig. 14B). This brief description of the CBL is consistent with results reported in many previous publications, as reviewed by Petrosyan et al. (2011) and Read et al. (2017).

Fig. 13 also shows the diurnal cycle of θ_{44}, the potential temperature on the forty-fourth level of the model (counting downward from the top) at about 1 km above ground level (AGL). There is a delay in the response of the atmosphere to surface forcing; θ_{44} reaches its peak value of 229 K at 16–17 h, about 3 h later than the peak in θ_s.

Finally, Fig. 13 compares the predicted diurnal cycles of θ_s and θ_{44} with results derived from observations at the same location. The measurements are at $L_s = 30°$, 10° earlier than the simulation. Nonetheless, the difference is less than 3 K in both cases. This comparison

confirms that each measurement (θ_s or θ_m) is at a local time near the peak in its diurnal cycle, as mentioned previously in Section 4.3.

6. Isidis regional study

This section focuses on the 36-km nest and the 17 RO profiles that sounded the atmosphere within this region. See Hinson (2018, doi:10.17632/kgvvmgvbnh.1) for electronic versions of these profiles. After validating the performance of the MMM by comparing simulated and measured profiles of θ (Section 6.1), we investigate the influence of the topographic circulation on the properties of the CBL (Section 6.2).

There appears to be little sol-to-sol variability among profiles at nearly the same location and local time in the tropics at this season. The repeatability of the measurements is illustrated by the pair of profiles from Lucus Planum in Fig. 5 as well as by the pairs of profiles from Amazonis and Isidis in Fig. 9. (Additional examples of repeatability appear in Section 6.1.) This conclusion is also supported by the mesoscale simulation, as noted in Section 5.1. We therefore assume that the differences among the 17 RO profiles arise entirely from spatial variations.

6.1. Validation of the MMM

We extracted a profile of θ from the 36-km nest at the location and local time sampled by each RO observation and used the method described in Section 3.1 to determine θ_m and D. For consistency with the RO measurements, the bottom 500 m of each simulated profile was excluded from the calculation of θ_m; this region, which includes the super-adiabatic surface layer, is inaccessible to the RO observations considered here. We characterized the surface forcing in the simulation by calculating θ_s at the local time of the TES dayside observations (14 h), as appropriate for comparisons with the RO results in Tables 2 and 3.

Fig. 15 compares RO and MMM profiles at locations outside the Isidis basin. The set of RO profiles in Fig. 15A includes one pair at low elevation ($z_s \approx -4.1$ km) in southwest Utopia Planitia and another pair at high elevation ($z_s \approx +1.7$ km) in southeast Syrtis Major. The CBL parameters for these four profiles are denoted by dark blue squares in Figs. 8A

and 8B; all four samples are close to the respective linear fits. Owing to a large increase in z_s (5.8 km) and a modest increase in T_s (4 K), θ_s is larger by about 37 K in southeast Syrtis, and both θ_m and D grow accordingly, by 28 K and 4 km, respectively.

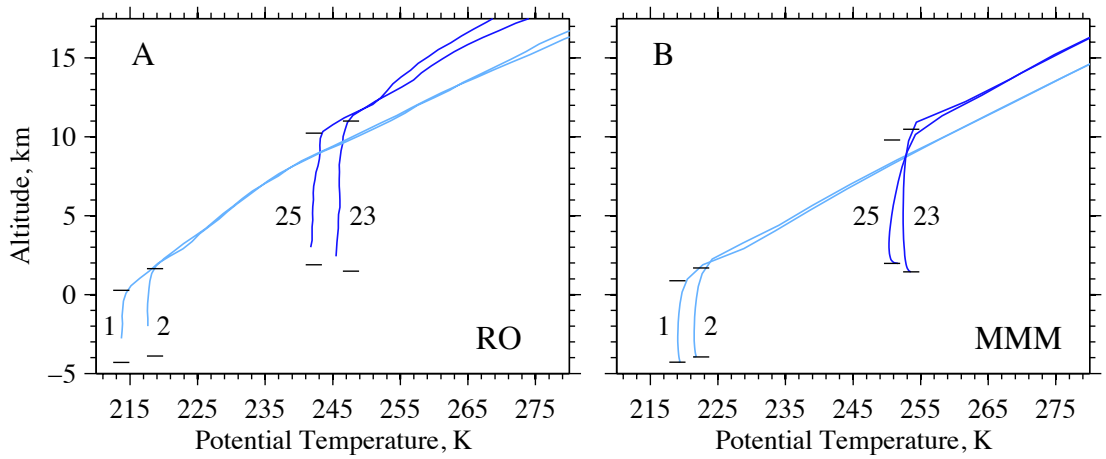

Figure 15: (A) RO profiles of θ in MY27. Profiles 1 and 2 are from southwest Utopia Planitia (107°E, 26°N, $L_s = 45°$); profiles 23 and 25 are from southeast Syrtis Major (73°E, 1°S, $L_s = 60°$). The interval between the first pair of observations is 3 sols; the second pair is separated by 6 sols. The local time is 17.1 h. (B) Profiles of θ at the same locations and local time from a simulation with the MMM at $L_s = 40°$. See Fig. 4 for further discussion.

The corresponding profiles from the MMM appear in Fig. 15B. There is a strong resemblance between the simulation and the observations. The change in surface forcing from Utopia to Syrtis causes the simulated values of θ_m and D to increase by 31 K and 3 km, respectively, comparable to the observed response. The most significant discrepancy is a warm bias of about 6 K in the simulated values of θ_m and a somewhat larger bias to θ in the free air above the CBL. We return to this point below.

Fig. 16 compares RO and MMM profiles from the southeast region of the nest. The CBL parameters for these three RO profiles are denoted by light blue squares in Figs. 8A and 8B. The surface forcing is essentially the same for each observation ($\theta_s \approx 261$ K), and there is close agreement among the values of θ_m (Fig. 8A). In contrast, the values of D are widely dispersed (Fig. 8B) and all three deviate from the linear fit (by +2.3 km for profile 19, −3.2

km for profile 24, and −1.8 km for profile 26).

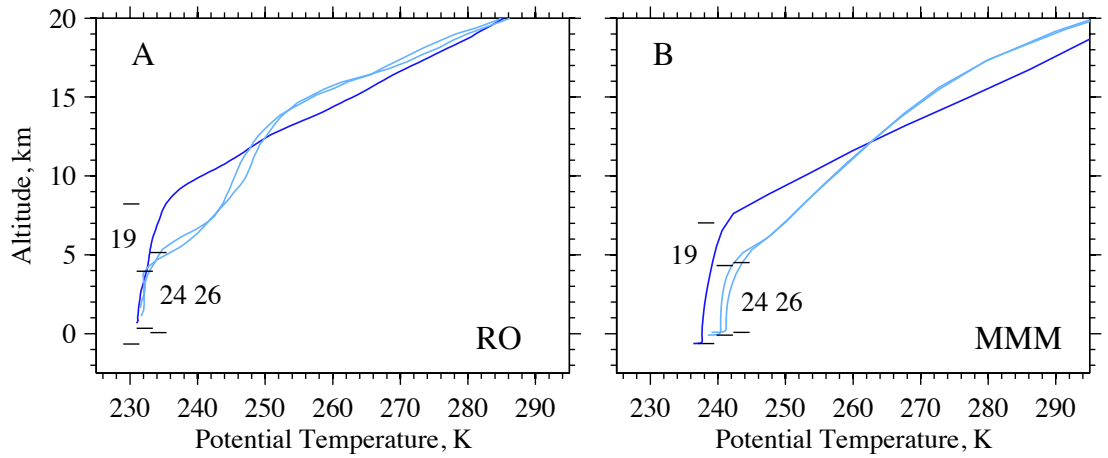

Figure 16: (A) RO profiles of θ in MY27. Profile 19 is from a location to the east of Isidis (106°E, 9°N, $L_s = 54°$); profiles 24 and 26 are from observations 3 sols apart at a location about 700 km farther south (106°E, 3°S, $L_s = 62°$). The local time is 17.1 h. (B) Profiles of θ at the same locations and local time from a simulation with the MMM at $L_s = 40°$. See Fig. 4 for further discussion.

The corresponding profiles from the MMM, which appear in Fig. 16B, capture the salient features of the RO profiles. There are notable similarities not only in the depth of the mixed layer but also in the structure of the overlying free air. As in Fig. 15, θ_m is warmer in the simulation than in the observations, in this case by about 8 K.

Fig. 17 compares RO and MMM profiles along an east-west line across the middle of the nest. The three RO profiles in Fig. 17A correspond to the blue squares in Figs. 8C and 8D. The CBL parameters are close to the respective linear fits with one exception — the mixed layer in profile 75 extends to 9.7 km above the surface, 2.5 km deeper than the linear fit in Fig. 8D. As noted previously in connection with Fig. 9, the free air immediately above the mixed layer is unusually warm in profile 74.

Fig. 17B shows the corresponding profiles from the MMM. Within the CBL, the simulation agrees closely with the observations — the warm bias in θ_m is only 3 K in this case, and the difference between the simulated and measured values of D does not exceed 0.8 km. The agreement is not as good in the free air above the mixed layer, where the difference

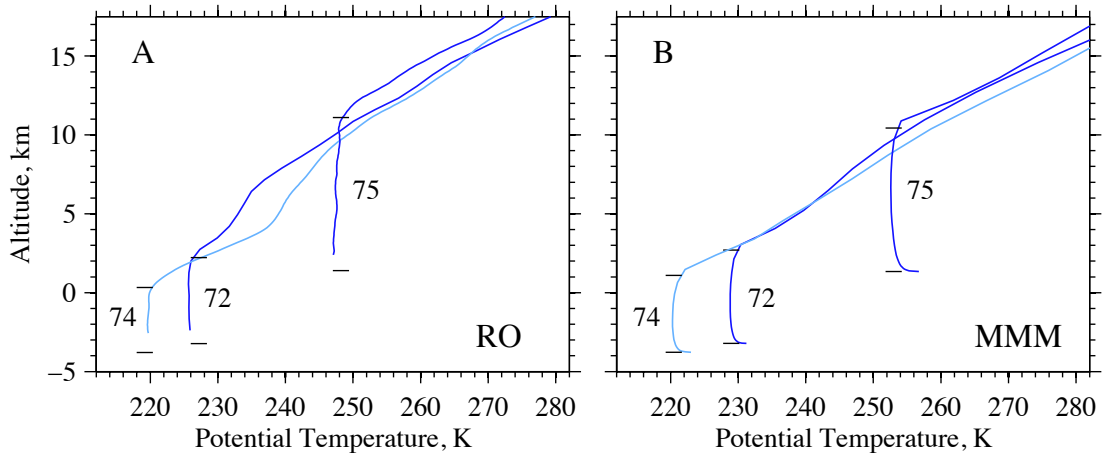

Figure 17: (A) RO profiles of θ from an 8-sol span of observations at $L_s = 32°$ of MY28. Profile 72 is from a location to the east of Isidis (118°E, 16°N); profile 74 is from a location near the center of Isidis (86°E, 14°N); profile 75 is from a location to the west of Isidis in Syrtis Major (55°E, 12°N). The local time is 15.8 h. (B) Profiles of θ at the same locations and local time from a simulation with the MMM at $L_s = 40°$. See Fig. 4 for further discussion.

between RO profiles 72 and 74 is absent from the simulation.

We evaluated the simulation more precisely by comparing its predictions with the measured values of D, θ_m, and θ_s at all 17 locations within the nest where RO profiles are available (Fig. 12). The differences — denoted as ΔD, $\Delta\theta_m$, and $\Delta\theta_s$ — are defined as positive when the simulated value is larger. The difference in the boundary layer parameters (ΔD and $\Delta\theta_m$) is computed at the local time of each RO observation; the difference in surface forcing ($\Delta\theta_s$) is computed at the local time of the MGS TES measurements of T_s.

The simulated values of D are consistent with the measurements, as shown in Fig. 18. The average value of ΔD is negligible. Its standard deviation is 0.8 km, comparable to the vertical resolution of the MMM profiles near the top of the CBL. Fig. 18 suggests that the simulation has a slight tendency to overestimate D when the mixed layer is shallow and underestimate D when the mixed layer is deep, but only by about 0.6 km in each case. These differences are more than ten times smaller than the range of D (3–12 km).

There is a seasonal trend in $\Delta\theta_m$; its value increases from about 2 K at $L_s = 30°$ to about

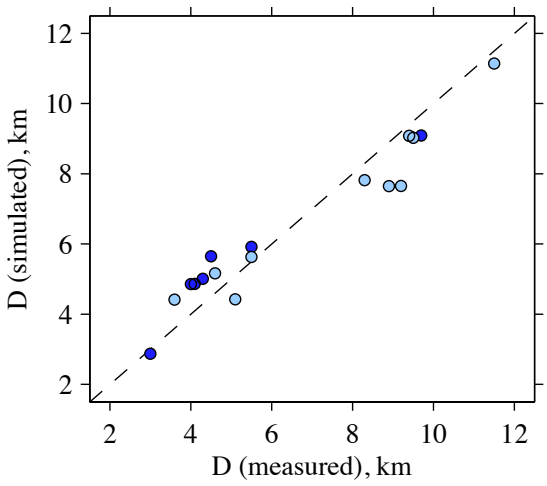

Figure 18: Comparison of simulated and measured values of D at the 17 locations shown in Fig. 12. Colors indicate measurements from (light blue) MY27 and (dark blue) MY28. The dashed line corresponds to perfect agreement.

8 K at $L_s = 60°$, as shown in Fig. 19. These differences are not surprising, given that the observations sampled a 37° range of L_s, whereas the simulation was performed at $L_s = 40°$. Both the seasonal trend and the bias in $\Delta\theta_m$ are probably associated with atmospheric dust, which has a strong effect on air temperature. In particular, the measurements of θ_m are affected by the annual decrease in dust opacity that begins in late winter and continues into late spring (Smith, 2004, Fig. 7).

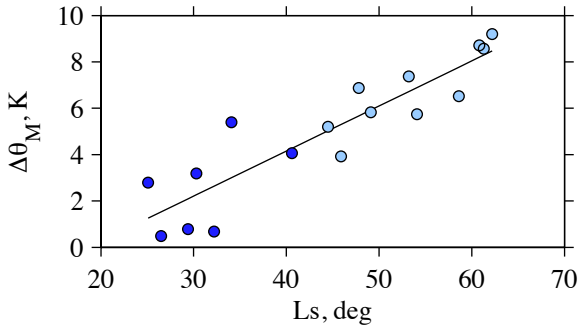

Figure 19: Comparison of simulated and measured values of θ_m at the 17 locations indicated in Fig. 12. Colors indicate measurements from (light blue) MY27 and (dark blue) MY28. The line is a least-squares fit.

The average value of $\Delta\theta_s$ is only -0.6 K and there is a seasonal trend much like the one in Fig. 19. In this case the trend arises from a misalignment in subsolar latitude ϕ_{ss}. For the RO observations in the Isidis region, ϕ_{ss} drifts from 10°N at $L_s = 25°$ to 22°N at $L_s = 62°$, whereas its value in the simulation is 16°N. This misalignment causes the measurements of T_s and θ_s to differ from the simulated values by as much as ± 5 K.

Finally, Fig. 20 shows the simulated response of the atmosphere to spatial variations in surface forcing. The dependence of θ_m on θ_s is linear; a least-squares fit has a slope α of 0.75 ± 0.04 and an intercept β of 39.2 ± 9.4 K, consistent with the RO measurements in Table 4. This implies that the model is providing a reasonably good representation of heat transport within the lower atmosphere.

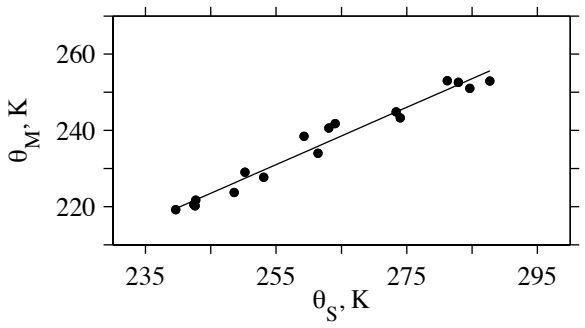

Figure 20: Response of θ_m to variations in θ_s as simulated by the MMM. Results are shown at the 17 locations indicated in Fig. 12. The line is a least-squares fit.

In summary, the results in Figs. 15–20 confirm key aspects of the simulation. The modest biases in θ_m and θ_s are not surprising for comparisons with observations that are distributed in L_s.

6.2. Simulation of the regional circulation

Topographic forcing produces a vigorous, diurnally varying circulation in the Isidis region. The winds affect both the structure and evolution of the CBL, most notably on the rim of Isidis.

The influence of topography on the regional circulation and the potential temperature of the mixed layer is illustrated in Fig. 21, which shows selected results from the 36-km nest

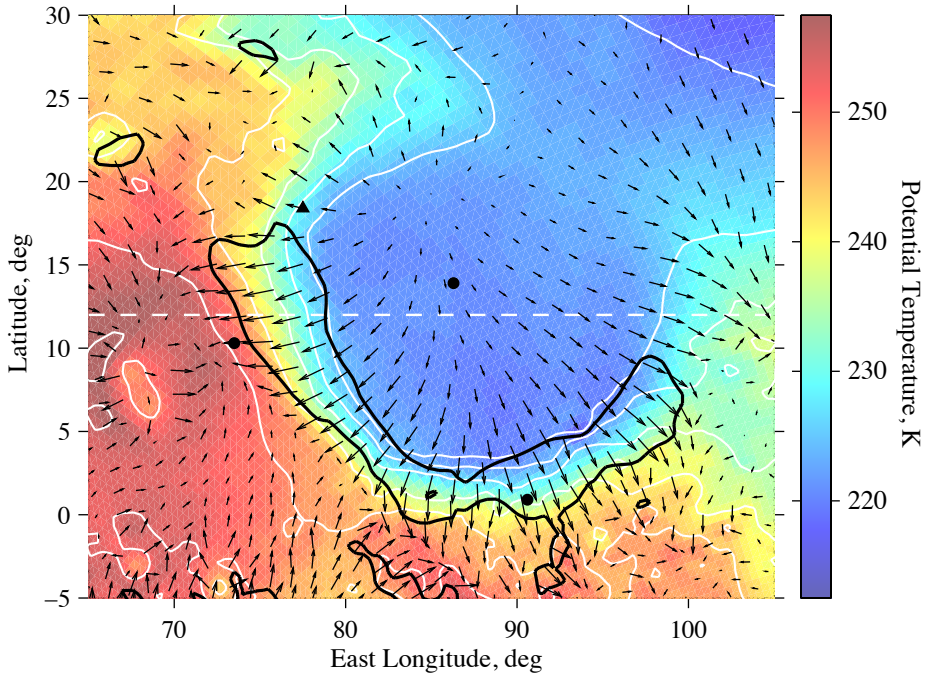

Figure 21: The simulated potential temperature and horizontal wind fields at 1 km AGL and 16 h local time. The length and orientation of the arrows indicate the wind speed and direction. Wind vectors are plotted at only one eighth of the grid points for clarity. The wind speed exceeds 13 m s^{-1} in areas enclosed by a black contour. The surface topography is shown by white contours at 1-km intervals. Black symbols mark the locations of three RO profiles (circles) and the JEZ landing site (triangle). The dashed white line is the location of the wind-field cross section in Fig. 22.

at 1 km AGL. The local time is constant (16 h), so that Universal Time varies by 1 h per 15° of longitude. Within Isidis, the wind vectors are generally radial and directed outward. The winds are strongest where the terrain is steep, on the western and southern boundaries of the basin, with upslope flow near the surface at this local time. The wind speed exceeds 13 m s^{-1} within a narrow, 180° arc along the circumference of the basin.

The wind vectors in Fig. 21 are superimposed on a color-coded map of θ_{44}, the potential temperature at 1 km AGL. At this local time there is a clear correlation between θ_{44} and surface elevation, as expected (see Section 4.3). This results in a strong gradient of θ_{44} where the topography is steep, while its value is more uniform within Isidis Planitia (about 222

K) and above the elevated terrain to the west of the basin (about 252 K).

Fig. 21 also shows the locations of RO profiles that sample three distinct regions: the central basin (profile 74 of MY28), the western rim (profile 15 of MY27), and the southern rim (profile 81 of MY28). Sections 6.2.1 and 6.2.2 examine the effect of the regional circulation on vertical profiles of θ at these locations.

A landing site in southern Isidis was once considered (but not selected) for the Mars Exploration Rovers (Golombek et al., 2003, Table 10). In support of mission planning, Rafkin and Michaels (2003) used a mesoscale model to predict the local state of the atmosphere during entry, descent, and landing. Their simulation was performed at $L_s = 320°$, when ϕ_{ss} is 16°S, significantly different than the case considered here ($L_s = 40°$ and $\phi_{ss} = 16°$N). Nonetheless, there is good qualitative agreement between basic features of the two simulations. For example, both models yield similar predictions for the near-surface wind field in midafternoon, with the strongest winds above the steep terrain along the western and southern boundaries of the Isidis basin (Rafkin and Michaels, 2003, Fig. 16b). In addition, the return flow into the basin produces afternoon subsidence in both simulations.

6.2.1. East-west transect

Fig. 22 shows longitude-height cross sections of the wind field at 12°N, which illustrate other aspects of the regional circulation. The location of this transect is indicated in Fig. 21; the local time is the same in both figures. Fig. 22 shows only the zonal (U) and vertical (W) components of the wind field. At this latitude, the meridional component (V) is less important to the regional circulation than U and W.

The afternoon winds in Fig. 22 arise primarily from topographic forcing. Near the western rim of Isidis, at about 70-80°E, there is strong, westward, upslope flow out of the basin at 0-5 km AGL, with U reaching -15 m s^{-1}. The return flow into the basin occurs at higher altitudes, at roughly 5-10 km AGL. Within this elevated layer, which slopes downward to the east, U and W reach $+15$ m s^{-1} and -0.4 m s^{-1}, respectively.

A mirror image of this circulation appears near the eastern rim, at about 95-105°E, with eastward, upslope flow at low altitudes and return flow at higher altitudes. However, the

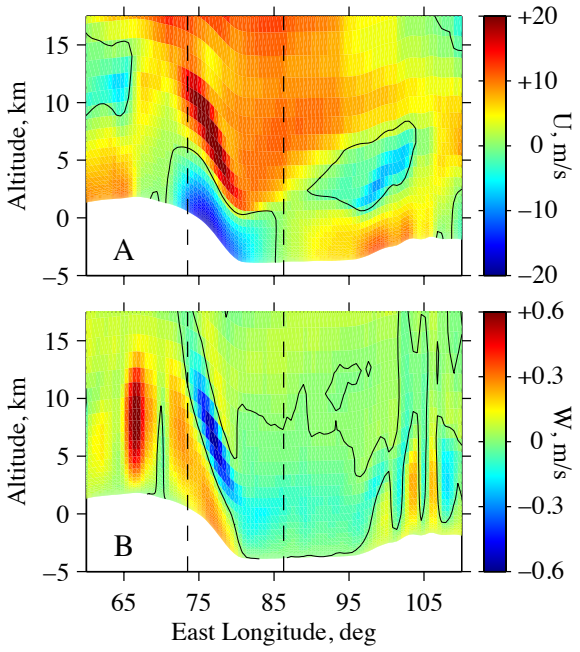

Figure 22: Longitude-height cross sections of the simulated wind field at 12°N. At this latitude, the two principal components of the regional circulation are (A) the zonal wind U (positive eastward) and (B) the vertical wind W (positive upward). The local time is 16 h. In both panels, the solid black line is the zero contour and the dashed vertical lines mark the longitudes of RO profiles 15 (73.5°E) and 74 (86.3°E). The white space at the bottom of each panel is the surface.

relatively shallow surface slope on the eastern boundary of the basin leads to a noticeably weaker circulation at that location. This asymmetry is even more pronounced to the northeast of Isidis, where the basin opens into Utopia Planitia and topographic forcing is largely absent. The resulting asymmetry of the regional circulation is apparent in Fig. 21.

At a local time of 16 h, rising motion along the rim of Isidis leads to widespread subsidence across the basin at altitudes below about 8 km (Fig. 22B). This coincides with the altitude range where RO profile 74 of MY28 — situated near the center of the basin at 86.3°E, 13.9°N — is notably warmer than a reference profile at the same latitude in Amazonis (Fig. 9). In Section 4.4 we tentatively attributed this warm layer to subsidence-induced adiabatic heating; the simulation provides qualitative support for this interpretation. However, the effects of adiabatic heating are more conspicuous in the observation than in the simulated

profile at this location (Fig. 17), which suggests that the model may be underestimating the rate of downward motion.

In Fig. 22, the strongest winds and the most dramatic spatial variations of the wind field occur along the western boundary of Isidis. Profile 15 of MY27 lies within this region at 73.5°E, 10.3°N; its peculiar appearance was discussed previously in connection with Fig. 10. To gain further insight, we now examine the time variation of the simulated winds in the vicinity of this observation.

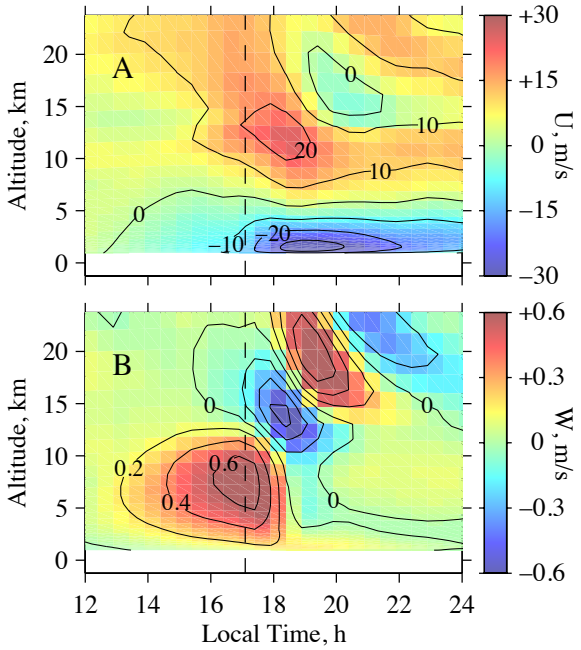

Figure 23: Variations with local time and altitude of (A) the zonal wind U and (B) the vertical wind W at 73.5°E, 10.3°N (profile 15 of MY27). This location is 100 km south of the transect in Fig. 21. The local time of the RO observation is 17.1 h, as indicated by a dashed vertical line in both panels. The contour interval is 10 m s^{-1} for U and 0.2 m s^{-1} for W. The white space at the bottom of each panel is the surface.

Fig. 23 shows the evolution of the simulated wind field between noon and midnight at the location of profile 15. The zonal winds strengthen after 16 h (Fig. 23A). Westward winds prevail at altitudes below 5 km, with U in excess of -30 m s^{-1} within 1 km of the surface at 18–20 h. Strong eastward winds appear at 10–15 km altitude. The vertical component of the wind field is generally directed upward in the afternoon (Fig. 23B). At altitudes below

608 12 km, W exceeds +0.2 m s^{-1} at 13–18 h, with a maximum of more than +0.6 m s^{-1} at
609 5–10 km altitude near 17 h. Horizontal and vertical winds of this magnitude can have a
610 large effect on profiles of θ.

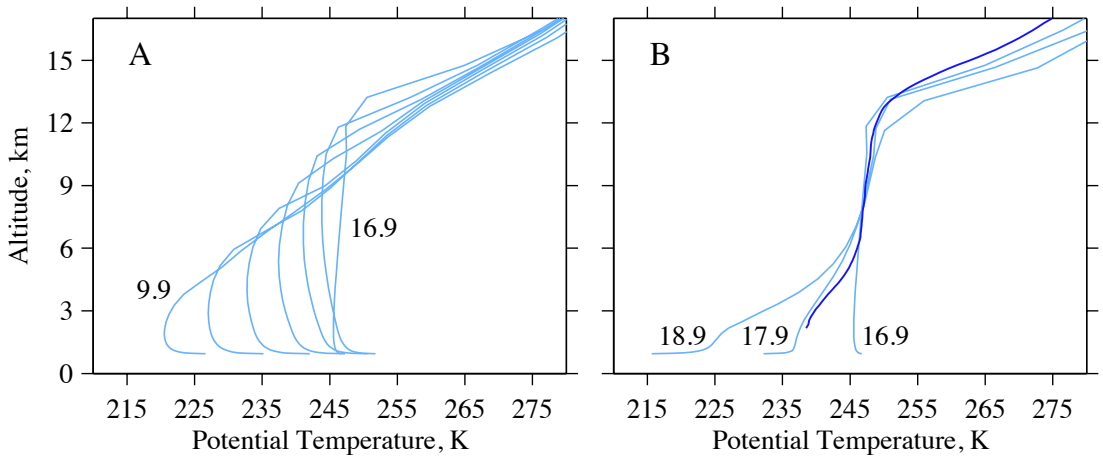

Figure 24: Profiles of θ at 73.5°E, 10.3°N. (A) Results from the mesoscale model are shown at 1-h intervals for local times of 9.9–16.9 h; the profile at 15.9 h was omitted for clarity. (B) Comparison of (light blue) simulated profiles at local times of 16.9, 17.9, and 18.9 h with (dark blue) RO profile 15. The local time of the observation is 17.1 h, about 1 h before sunset (18.2 h). The surface elevation is 1.0 km. The bias in θ_m has been removed from the simulated profiles in both panels.

611 The simulation accounts for two distinctive characteristics of RO profile 15, as shown
612 in Fig. 24, which compares simulated profiles of θ with the observation. First, the CBL is
613 unusually deep at this location. The measured value of D (11.5 km) is 2.6 km larger than the
614 linear fit in Fig. 8B, as shown by the orange square. The simulation produces a comparably
615 deep CBL (Fig. 24B), which arises in part from strong, upward winds at altitudes below
616 about 12 km (Fig. 23B). This upward motion causes θ to decrease steadily throughout the
617 afternoon at altitudes of 9–13 km (Fig. 24A), which in turn enables convective mixing to
618 extend to higher altitudes than it ordinarily would. See Fig. 14A for a contrasting case
619 where the vertical winds are too weak to influence the depth of the CBL.

620 The second distinctive characteristic of RO profile 15 is the presence of stable stratifica-
621 tion at altitudes below 6 km. The simulated profiles exhibit a rapid, early evening decrease

of θ in this altitude range (Fig. 24B); at 1 km AGL, the peak cooling rate is 13 K h^{-1} at 18 h. This cooling is contemporaneous with the early evening, westward surge in U at low altitudes (Fig. 23A), which reduces θ through horizontal advection of cool air, as discussed below. There is a close resemblance between the simulated profile at 17.9 h and the structure observed nearly 1 h earlier at 17.1 h (Fig. 24B); we return to this point after further discussion of the cooling mechanism.

Fig. 25 provides context for understanding the results in Fig. 24B. It shows the simulated wind and potential temperature fields at 1 km AGL, as in Fig. 21, but the local time is 19 h rather than 16 h. The wind direction is similar at the two local times, with strong upslope flow along the western and southern boundaries of Isidis. However, the wind speed has increased significantly at 19 h and the region where the winds are strongest has moved outward from the basin. This early evening surge in the near-surface winds occurs after the surface layer has vanished. In the absence of heating from below, an air parcel moving out of the basin remains at nearly constant θ, so that upslope advection replaces high-θ air that previously occupied the rim (Fig. 21) with low-θ air from the basin. Expressed in another way (Andrews et al., 1987, Section 3.2),

$$\partial\theta/\partial t \approx -\left(U\partial\theta/\partial x + V\partial\theta/\partial y\right) , \tag{5}$$

where x and y are eastward and northward Cartesian coordinates, and $\partial\theta/\partial t$ is the time derivative at a fixed location. Advection causes rapid cooling near the surface along the western rim, where θ_{44} decreases by about 20 K between the leading and trailing edges of the 20 m s^{-1} wind contour in Fig. 25. At the location of RO profile 15, the simulated near-surface temperature drops precipitously at local times of 17–20 h; the RO profile generally confirms this aspect of the simulation. The same type of low-altitude cooling also occurs in the simulation at the location of RO profile 23 (marked in Fig. 25), but it begins about 3 h later owing to the increase in distance from the basin.

The RO profile in Fig. 24B suggests that near-surface cooling begins nearly 1 h sooner than in the simulation. Several factors could be responsible for this discrepancy, such as the horizontal resolution of the RO profile (Fig. 12) and the 13° offset in L_s between the

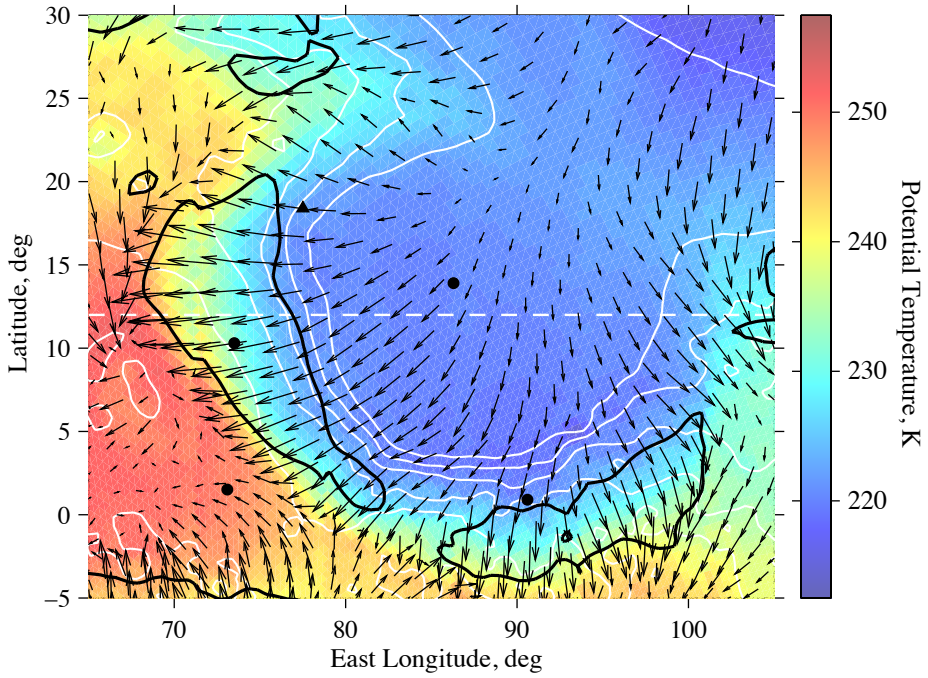

Figure 25: The simulated potential temperature and horizontal wind fields at 1 km AGL and 19 h local time. The format is the same as in Fig. 21 with two exceptions. First, the black contour now encloses regions where the wind speed exceeds 20 m s^{-1} rather than 13 m s^{-1}. Second, a symbol has been added to mark the location of RO profile 23 of MY27 (circle at lower left). However, the normalization applied to the length of the wind vectors is the same in both figures; the winds are much stronger at the local time shown here.

simulation and the observation. In addition, the accuracy of the simulation might be affected by uncertainties in surface properties, particularly the aerodynamic roughness, which was assumed to be spatially uniform with a value of 0.01 m in this simulation. Small-scale roughness can have a significant impact on the near-surface wind field.

At locations far removed from the rim of Isidis, θ decreases much more gradually at sunset. For example, the early evening cooling rate at 1 km AGL is less than 2 K h^{-1} in Elysium Planitia (Fig. 14B) as compared with more than 10 K h^{-1} on the western rim (Fig. 24B). These two locations are labeled as 72 and 15, respectively, in Fig. 12.

6.2.2. The southern rim

Unusual structure also appears in RO profile 81 of MY28 (Fig. 10). This observation is on the southern rim of Isidis, as shown in Figs. 12, 21, and 25, where the principal components of the regional circulation are the meridional wind V and the vertical wind W.

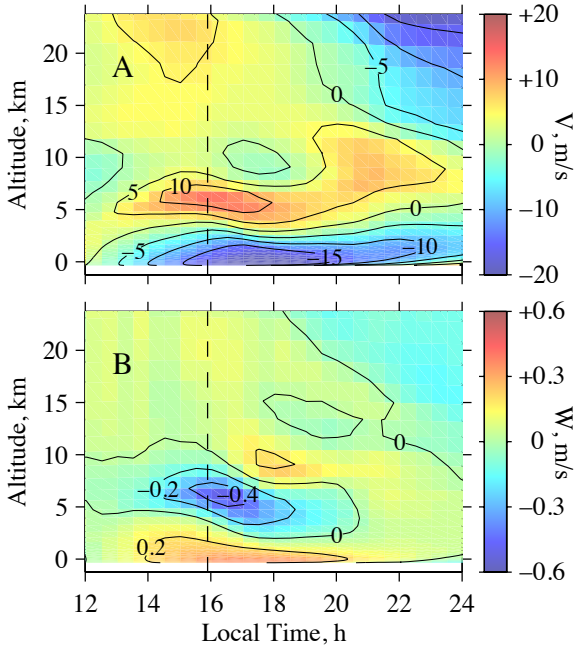

Figure 26: Variations with local time and altitude of the winds at 90.6°E, 0.9°N (profile 81 of MY28). At this location the principal components of the regional circulation are (A) the meridional wind V (positive northward) and (B) the vertical wind W (positive upward). The local time of the RO observation is 15.9 h, as indicated by a dashed vertical line in both panels. The contour interval is 5 m s^{-1} for V and 0.2 m s^{-1} for W. The white space at the bottom of each panel is the surface.

The time variation of the simulated wind field on the southern rim is similar to what occurs on the western rim, though somewhat weaker, as shown in Fig. 26. On the southern rim, upslope flow out of Isidis generates southward winds at altitudes below 3 km (Fig. 26A), where V reaches -15 m s^{-1} at local times of 15–20 h. The return flow into the basin occurs at 4–8 km altitude, where V is about $+10$ m s^{-1} at local times of 14–18 h. The vertical winds at this location are downward at 3–9 km altitude in mid-to-late afternoon, peaking at about -0.4 m s^{-1}, with weaker upward motion of about $+0.2$ m s^{-1} at altitudes below 3

669 km (Fig. 26B).

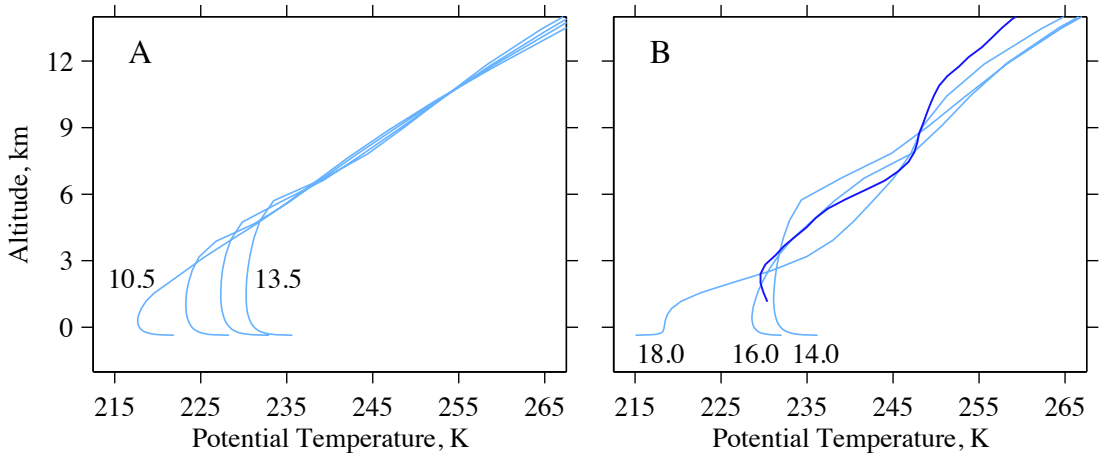

Figure 27: Profiles of θ at 90.6°E, 0.9°N. (A) Results from the mesoscale model are shown at 1-h intervals for local times of 10.5–13.5 h. (B) Comparison of (light blue) simulated profiles at local times of 14.0, 16.0, and 18.0 h with (dark blue) RO profile 81. The local time of the observation is 15.9 h, about 2 h before sunset (18.0 h). The surface elevation is −0.4 km. The bias in θ_m has been removed from the simulated profiles in both panels.

670 Fig. 27 shows simulated profiles of θ at the location of RO profile 81. At local times
671 before 14 h, when the vertical winds are relatively weak (Fig. 26B), the evolution of the
672 CBL is unremarkable (Fig. 27A), and it resembles the midday segment of the diurnal cycle
673 in Elysium Planitia (Fig. 14A). The situation changes markedly in midafternoon with the
674 onset of stronger vertical winds. Downward winds at 3–9 km altitude produce adiabatic
675 warming that inhibits convection and reduces the depth of the CBL (Fig. 27B). The sim-
676 ulated profile at 16 h mimics the structure observed at 15.9 h, implying that the vertical
677 winds are responsible for the unusually shallow CBL observed at this location. The mea-
678 sured value of D (3.0 km) is 2.5 km smaller than the linear fit in Fig. 8D, as indicated by
679 the orange square.

680 At local times after 16 h, the simulated profiles in Fig. 27B cool rapidly near the surface.
681 This arises from the early evening surge of cool air out of the Isidis basin (Fig. 25), as
682 discussed above. The peak cooling rate on the southern rim is about 5 K h^{-1}, less than half

as large as on the western rim.

In summary, both vertical motion and horizontal advection have a significant impact on the structure and evolution of the CBL on the rim of Isidis, as illustrated in Figs. 24 and 27. These comparisons confirm several aspects of the simulated wind field.

7. Summary and Discussion

7.1. Observations

We have characterized basic properties of the late-afternoon CBL through analysis of MEx RO profiles. The observations cover latitudes from 55°N to 14°S in northern spring of MY27 and MY28. The spatial coverage of the two datasets is complementary (Fig. 1). The new results from MY28 (Table 2) greatly increase the total number of CBL measurements and extend the sampling to a wide variety of conditions (z_s and T_s).

The measurements from MY27 were analyzed previously by Hinson et al. (2008), who identified a strong correlation between surface elevation and CBL depth. This dependence, known as the pressure effect, is also evident in large-eddy simulations (Spiga et al., 2010a,b). We have extended the previous work by adopting a more general definition of surface forcing (θ_s in Eq. (2)), which yields an improved characterization of the behavior of the CBL (Fig. 8, Table 4). Our analysis confirms that the mixed layer is generally deeper where the surface forcing is stronger, but outliers from the linear fits in Figs. 8B and 8D indicate that the depth of the mixed layer is not controlled by surface forcing alone.

For the observations considered here, the average value of $\theta_s - \theta_m$ is about 30 K in both MY27 and MY28. A large part of this temperature difference originates from two constraints on the thermal coupling between the surface and the surface layer (Ye et al., 1990; Haberle et al., 1993; Savijärvi, 1999). First, the surface layer absorbs only part of the upwelling infrared radiation from the ground, mainly in the 15-μm band of CO_2; the rest is absorbed over an extended altitude range or lost to space. Second, the sensible heat flux from the ground is inhibited by the low density of the Martian atmosphere. Temperature measurements by the Mars Exploration Rover in Meridiani Planum illustrate the importance

of these two effects — the air 1 m above the ground is about 25 K colder than the surface at the local time of the measurements in Fig. 8 (Smith et al., 2004, Fig. 3).

Our analysis reveals another important property of the CBL. The variation of θ_m with θ_s is nearly linear across a broad range of surface conditions, with a well-defined, characteristic slope of 0.72 ± 0.04 in MY27 and 0.71 ± 0.03 in MY28 (Eq. (4) and Table 4). The slope is a consequence of restrictions on the efficiency of daytime heat transport from the surface, through the shallow, super-adiabatic surface layer, and into the overlying mixed layer. This result provides a new benchmark for testing the performance of general circulation models, mesoscale models, and large-eddy simulations.

7.2. Modeling

We performed a numerical simulation with the OSU MMM at $L_s = 40°$ to investigate the mesoscale meteorology in the vicinity of Isidis Planitia, a region that includes two potential landing sites for the Mars 2020 Rover. We validated the simulation through detailed comparisons with RO profiles and measured values of θ_m and D (Section 6.1); in most respects the simulation agrees closely with the observations. Fig. 12 shows the validated map of CBL depth in the Isidis region.

Mars 2020 is relying on the MMM along with a second mesoscale model (Rafkin et al., 2001; Rafkin and Michaels, 2003) to predict the state of the atmosphere at $L_s = 6°$, when the rover will descend to the surface. By confirming the accuracy of the MMM under similar conditions, the results reported here indirectly support this aspect of mission planning.

We used the Isidis regional simulation to explore the topographic circulation associated with this large impact basin (Section 6.2). Comparisons between MMM predictions and RO observations yield two important conclusions. First, a low-altitude surge of cool air from the Isidis basin causes θ to decrease rapidly in the early evening on the western rim (Fig. 24B). Second, the diurnally varying circulation can strongly influence the depth of the mixed layer. Subsidence increases the temperature in the free air and restricts the depth of the CBL (Fig. 27B); upward motion has the opposite effect (Fig. 24A). The regional circulation thereby suppresses the depth of the CBL at some locations while enhancing it at others. In

the Isidis region, these wind-induced changes in D are comparable to those produced by the pressure effect.

7.3. Future work

MEx will continue to monitor the atmosphere of Mars as part of its ongoing extended mission. A campaign of RO observations in August–November 2018 ($L_s \approx 260°$), which began while this paper was under review, is filling a notable gap in RO coverage by sampling the late-afternoon structure of the CBL in the southern hemisphere (10–55°S). The resulting RO profiles will be used to investigate the regional circulation associated with large, midlatitude impact basins such as Hellas and Argyre.

Acknowledgments. We are indebted to the European Space Agency (ESA) for conducting the highly successful Mars Express mission; to the National Aeronautics and Space Administration (NASA) for its contributions to the mission; to the personnel of the NASA Deep Space Network (DSN) and the European Space Tracking Network (ESTRACK) for maintaining, scheduling, and operating the ground equipment used for RO measurements; to Daniel Kahan of the Radio Science Systems Group at the Jet Propulsion Laboratory (JPL) for configuring and operating the DSN receivers; to Richard Simpson at Stanford University for monitoring data quality and maintaining a meticulous archive of DSN data products; and to Tommy Thompson at JPL for management and guidance of US participants in the Mars Express mission. This research was funded by the NASA Mars Exploration Program, which supports the US investigators on Mars Express; by the NASA Mars Critical Data Products Program; and by the German Aerospace Center (DLR).

References

Andrews, D. G., Holton, J. R., Leovy, C. B., 1987. Middle Atmosphere Dynamics. Elsevier, New York.

Benson, J. L., James, P. B., 2003. Yearly Comparisons of the Mars North Polar Cap: 1999, 2001, and 2003 MOC Observations. In: Clifford, S., Doran, P., Fisher, D., Herd, C. (Eds.), Third International Conference on Mars Polar Science and Exploration. p. 8097.

Brandt, S., 1989. Statistical and computational methods in data analysis. Amsterdam: North-Holland, 1976, 2nd rev. ed., 5th repr. 1989.

Christensen, P. R., Bandfield, J. L., Hamilton, V. E., Ruff, S. W., Kieffer, H. H., Titus, T. N., Malin, M. C., Morris, R. V., Lane, M. D., Clark, R. L., Jakosky, B. M., Mellon, M. T., Pearl, J. C., Conrath, B. J., Smith, M. D., Clancy, R. T., Kuzmin, R. O., Roush, T., Mehall, G. L., Gorelick, N., Bender, K., Murray, K., Dason, S., Greene, E., Silverman, S., Greenfield, M., 2001. Mars Global Surveyor Thermal Emission Spectrometer experiment: Investigation description and surface science results. Journal of Geophysical Research 106, 23823–23872.

Clancy, R. T., Sandor, B. J., Wolff, M. J., Christensen, P. R., Smith, M. D., Pearl, J. C., Conrath, B. J., Wilson, R. J., 2000. An intercomparison of ground-based millimeter, MGS TES, and Viking atmospheric temperature measurements: Seasonal and interannual variability of temperatures and dust loading in the global Mars atmosphere. Journal of Geophysical Research 105, 9553–9572.

Conrath, B. J., Pearl, J. C., Smith, M. D., Maguire, W. C., Christensen, P. R., Dason, S., Kaelberer, M. S., 2000. Mars Global Surveyor Thermal Emission Spectrometer (TES) observations: Atmospheric temperatures during aerobraking and science phasing. Journal of Geophysical Research 105, 9509–9520.

Gill, A. E., 1982. Atmosphere-Ocean Dynamics. Academic Press, San Diego.

Golombek, M. P., Grant, J. A., Parker, T. J., Kass, D. M., Crisp, J. A., Squyres, S. W., Haldemann, A. F. C., Adler, M., Lee, W. J., Bridges, N. T., Arvidson, R. E., Carr, M. H., Kirk, R. L., Knocke, P. C., Roncoli, R. B., Weitz, C. M., Schofield, J. T., Zurek, R. W., Christensen, P. R., Fergason, R. L., Anderson, F. S., Rice, J. W., 2003. Selection of the Mars Exploration Rover landing sites. Journal of Geophysical Research (Planets) 108, 8072.

Haberle, R. M., Houben, H. C., Hertenstein, R., Herdtle, T., 1993. A boundary-layer model for Mars - Comparison with Viking lander and entry data. Journal of Atmospheric Sciences 50, 1544–1559.

Haberle, R. M., Joshi, M. M., Murphy, J. R., Barnes, J. R., Schofield, J. T., Wilson, G., Lopez-Valverde, M., Hollingsworth, J. L., Bridger, A. F. C., Schaeffer, J., 1999. General circulation model simulations of the Mars Pathfinder atmospheric structure investigation/meteorology data. Journal of Geophysical Research (Planets) 104, 8957–8974.

Hinson, D. P., 2018. Mars Express radio occultation measurements of the Martian daytime convective boundary layer. Mendeley Data, v1, http://dx.doi.org/10.17632/kgvvmgvbnh.1.

793 Hinson, D. P., Asmar, S. W., Kahan, D. S., Akopian, V., Haberle, R. M., Spiga, A., Schofield, J. T.,
794 Kleinböhl, A., Abdou, W. A., Lewis, S. R., Paik, M., Maalouf, S. G., 2014. Initial results from radio
795 occultation measurements with the Mars Reconnaissance Orbiter: A nocturnal mixed layer in the tropics
796 and comparisons with polar profiles from the Mars Climate Sounder. Icarus 243, 91–103.
797 Hinson, D. P., Pätzold, M., Tellmann, S., Häusler, B., Tyler, G. L., 2008. The depth of the convective
798 boundary layer on Mars. Icarus 198, 57–66.
799 Hinson, D. P., Simpson, R. A., Twicken, J. D., Tyler, G. L., Flasar, F. M., 1999. Initial results from radio
800 occultation measurements with Mars Global Surveyor. Journal of Geophysical Research 104, 26997–27012.
801 Hinson, D. P., Wilson, R. J., 2004. Temperature inversions, thermal tides, and water ice clouds in the
802 Martian tropics. Journal of Geophysical Research (Planets) 109, E01002.
803 Hong, S.-Y., Pan, H.-L., 1996. Nonlocal Boundary Layer Vertical Diffusion in a Medium-Range Forecast
804 Model. Monthly Weather Review 124, 2322–2339.
805 Kleinböhl, A., Schofield, J. T., Kass, D. M., Abdou, W. A., Backus, C. R., Sen, B., Shirley, J. H., Lawson,
806 W. G., Richardson, M. I., Taylor, F. W., Teanby, N. A., McCleese, D. J., 2009. Mars Climate Sounder
807 limb profile retrieval of atmospheric temperature, pressure, and dust and water ice opacity. Journal of
808 Geophysical Research (Planets) 114, E10006.
809 Lewis, S. R., Mulholland, D. P., Read, P. L., Montabone, L., Wilson, R. J., Smith, M. D., 2016. The solsticial
810 pause on Mars: 1. A planetary wave reanalysis. Icarus 264, 456–464.
811 Lindal, G. F., Hotz, H. B., Sweetnam, D. N., Shippony, Z., Brenkle, J. P., Hartsell, G. V., Spear, R. T.,
812 Michael, Jr., W. H., 1979. Viking radio occultation measurements of the atmosphere and topography of
813 Mars - Data acquired during 1 Martian year of tracking. Journal of Geophysical Research 84, 8443–8456.
814 McCleese, D. J., Heavens, N. G., Schofield, J. T., Abdou, W. A., Bandfield, J. L., Calcutt, S. B., Irwin,
815 P. G. J., Kass, D. M., Kleinböhl, A., Lewis, S. R., Paige, D. A., Read, P. L., Richardson, M. I., Shirley,
816 J. H., Taylor, F. W., Teanby, N., Zurek, R. W., 2010. Structure and dynamics of the Martian lower
817 and middle atmosphere as observed by the Mars Climate Sounder: Seasonal variations in zonal mean
818 temperature, dust, and water ice aerosols. Journal of Geophysical Research (Planets) 115(E12), 12016.
819 Pätzold, M., Häusler, B., Tyler, G. L., Andert, T., Asmar, S. W., Bird, M. K., Dehant, V., Hinson,
820 D. P., Rosenblatt, P., Simpson, R. A., Tellmann, S., Withers, P., Beuthe, M., Efimov, A. I., Hahn, M.,
821 Kahan, D., Le Maistre, S., Oschlisniok, J., Peter, K., Remus, S., 2016. Mars Express 10 years at Mars:
822 Observations by the Mars Express Radio Science Experiment (MaRS). Planetary and Space Science 127,
823 44–90.
824 Petrosyan, A., Galperin, B., Larsen, S. E., Lewis, S. R., Määttänen, A., Read, P. L., Renno, N., Rogberg,
825 L. P. H. T., Savijärvi, H., Siili, T., Spiga, A., Toigo, A., Vázquez, L., 2011. The Martian Atmospheric
826 Boundary Layer. Reviews of Geophysics 49, RG3005.

827 Putzig, N. E., Mellon, M. T., Kretke, K. A., Arvidson, R. E., 2005. Global thermal inertia and surface
828 properties of Mars from the MGS mapping mission. Icarus 173, 325–341.
829 Rafkin, S. C. R., Haberle, R. M., Michaels, T. I., 2001. The Mars Regional Atmospheric Modeling System:
830 Model Description and Selected Simulations. Icarus 151, 228–256.
831 Rafkin, S. C. R., Michaels, T. I., 2003. Meteorological predictions for 2003 Mars Exploration Rover high-
832 priority landing sites. Journal of Geophysical Research (Planets) 108, 8091.
833 Read, P. L., Galperin, B., Larsen, S. E., Lewis, S. R., Määttänen, A., Petrosyan, A., Rennó, N., Savijärvi,
834 H., Siili, T., Spiga, A., Toigo, A., Vázquez, L., 2017. The Martian Planetary Boundary Layer. In:
835 R. M. Haberle (Ed.), The Atmosphere and Climate of Mars. Cambridge University Press, New York,
836 pp. 172–202.
837 Rosenblatt, P., Lainey, V., Le Maistre, S., Marty, J. C., Dehant, V., Pätzold, M., Van Hoolst, T., Häusler,
838 B., 2008. Accurate Mars Express orbits to improve the determination of the mass and ephemeris of the
839 Martian moons. Planetary and Space Science 56, 1043–1053.
840 Savijärvi, H., 1999. A model study of the atmospheric boundary layer in the Mars Pathfinder lander condi-
841 tions. Quarterly Journal of the Royal Meteorological Society 125, 483–493.
842 Schofield, J. T., Barnes, J. R., Crisp, D., Haberle, R. M., Larsen, S., Magalhaes, J. A., Murphy, J. R., Seiff,
843 A., Wilson, G., 1997. The Mars Pathfinder Atmospheric Structure Investigation/Meteorology. Science
844 278, 1752–1758.
845 Smith, D. E., Zuber, M. T., Frey, H. V., Garvin, J. B., Head, J. W., Muhleman, D. O., Pettengill, G. H.,
846 Phillips, R. J., Solomon, S. C., Zwally, H. J., Banerdt, W. B., Duxbury, T. C., Golombek, M. P., Lemoine,
847 F. G., Neumann, G. A., Rowlands, D. D., Aharonson, O., Ford, P. G., Ivanov, A. B., Johnson, C. L.,
848 McGovern, P. J., Abshire, J. B., Afzal, R. S., Sun, X., 2001. Mars Orbiter Laser Altimeter: Experiment
849 summary after the first year of global mapping of Mars. Journal of Geophysical Research 106, 23,689–
850 23,722.
851 Smith, M. D., 2004. Interannual variability in TES atmospheric observations of Mars during 1999-2003.
852 Icarus 167, 148–165.
853 Smith, M. D., Wolff, M. J., Lemmon, M. T., Spanovich, N., Banfield, D., Budney, C. J., Clancy, R. T.,
854 Ghosh, A., Landis, G. A., Smith, P., Whitney, B., Christensen, P. R., Squyres, S. W., 2004. First
855 Atmospheric Science Results from the Mars Exploration Rovers Mini-TES. Science 306, 1750–1753.
856 Smith, M. D., Wolff, M. J., Spanovich, N., Ghosh, A., Banfield, D., Christensen, P. R., Landis, G. A.,
857 Squyres, S. W., 2006. One Martian year of atmospheric observations using MER Mini-TES. Journal of
858 Geophysical Research (Planets) 111(E10), E12S13.
859 Spiga, A., Forget, F., Lewis, S. R., Hinson, D. P., 2010a. Structure and dynamics of the convective bound-
860 ary layer on Mars as inferred from large-eddy simulations and remote-sensing measurements. Quarterly

861 Journal of the Royal Meteorological Society 136, 414–428.
862 Spiga, A., Forget, F., Lewis, S. R., Hinson, D. P., 2010b. Correction to: 'Structure and dynamics of the
863 convective boundary layer on Mars as inferred from large-eddy simulations and remote-sensing measure-
864 ments'. Quarterly Journal of the Royal Meteorological Society 136, 2205–2206.
865 Tellmann, S., Pätzold, M., Häusler, B., Hinson, D. P., Tyler, G. L., 2013. The structure of Mars lower
866 atmosphere from Mars Express Radio Science (MaRS) occultation measurements. Journal of Geophysical
867 Research (Planets) 118, 306–320.
868 Toigo, A. D., Richardson, M. I., 2003. Meteorology of proposed Mars Exploration Rover landing sites.
869 Journal of Geophysical Research (Planets) 108, 8092.
870 Tyler, D., Barnes, J. R., 2005. A mesoscale model study of summertime atmospheric circulations in the
871 north polar region of Mars. Journal of Geophysical Research (Planets) 110, E06007.
872 Tyler, D., Barnes, J. R., 2013. Mesoscale Modeling of the Circulation in the Gale Crater Region: An
873 Investigation into the Complex Forcing of Convective Boundary Layer Depths. International Journal of
874 Mars Science and Exploration 8, 58–77.
875 Tyler, D., Barnes, J. R., 2015. Convergent crater circulations on Mars: Influence on the surface pressure
876 cycle and the depth of the convective boundary layer. Geophysical Research Letters 42, 7343–7350.
877 Tyler, D., Barnes, J. R., Haberle, R. M., 2002. Simulation of surface meteorology at the Pathfinder and VL1
878 sites using a Mars mesoscale model. Journal of Geophysical Research (Planets) 107, 5018.
879 Tyler, D., Barnes, J. R., Skyllingstad, E. D., 2008. Mesoscale and large-eddy simulation model studies of
880 the Martian atmosphere in support of Phoenix. Journal of Geophysical Research (Planets) 113, E00A12.
881 Vasavada, A. R., Chen, A., Barnes, J. R., Burkhart, P. D., Cantor, B. A., Dwyer-Cianciolo, A. M., Fergason,
882 R. L., Hinson, D. P., Justh, H. L., Kass, D. M., Lewis, S. R., Mischna, M. A., Murphy, J. R., Rafkin,
883 S. C. R., Tyler, D., Withers, P. G., Sep. 2012. Assessment of Environments for Mars Science Laboratory
884 Entry, Descent, and Surface Operations. Space Science Reviews 170, 793–835.
885 Wang, H., Zurek, R. W., Richardson, M. I., 2005. Relationship between frontal dust storms and transient
886 eddy activity in the northern hemisphere of Mars as observed by Mars Global Surveyor. Journal of
887 Geophysical Research (Planets) 110(E9), E07005.
888 Ye, Z. J., Segal, M., Pielke, R. A., 1990. A comparative study of daytime thermally induced upslope flow
889 on Mars and Earth. Journal of Atmospheric Sciences 47, 612–628.